Spatiotemporal orchestration of multicellular transcriptional programs and communications in the early stage of spinal cord injury

Zeqing Wang[1,5,6], Zhuxia Li[2,5,6], Tianle Luan[1,5], Guizhong Cui[4], Shunpan Shu[1,5], Yiyao Liang[3], Jingshu Xiao[4], Kai Zhang[1,5], Wei Yu[3], Jihong Cui[1], Ang Li[3,4,*], Guangdun Peng[2,4,5,*], and Yanshan Fang[1,5,*]

[1]Interdisciplinary Research Center on Biology and Chemistry, Shanghai Institute of Organic Chemistry, Chinese Academy of Sciences, Shanghai, 201210, China

[2]Center for Cell Lineage and Development, CAS Key Laboratory of Regenerative Biology, Guangdong Provincial Key Laboratory of Stem Cell and Regenerative Medicine, GIBH-HKU Guangdong-Hong Kong Stem Cell and Regenerative Medicine Research Centre, Guangzhou Institutes of Biomedicine and Health, Chinese Academy of Sciences, Guangzhou, 510530, China

[3]Guangdong-Hong Kong-Macau Institute of CNS Regeneration, Key Laboratory of CNS Regeneration of Ministry of Education, Jinan University, Guangzhou, 510632, China

[4]Bioland Laboratory (Guangzhou Regenerative Medicine and Health Guangdong Laboratory), Guangzhou, 510005, China

[5]University of Chinese Academy of Sciences, Beijing, 100049, China

[6]These authors contributed equally to this work

***Co-corresponding authors**:

Ang Li: anglijnu@jnu.edu.cn, ORCID: 0000-0002-9886-4880

Guangdun Peng: peng_guangdun@gibh.ac.cn, ORCID: 0000-0002-8586-0637

Yanshan Fang: fangys@sioc.ac.cn, ORCID: 0000-0002-4123-0174

Running title: Spatial transcriptomics of SCI

Keywords: RNA-seq; spatial transcriptomics; spinal cord injury; neuroimmune; neuroinflammation; astrocytes.

Word counts: ~7,200 words (*excluding the title page, methods, acknowledgements and references)*

ABSTRACT (*≤200 words*):

While spinal cord injury (SCI) involves a complex cascade of cellular and pathological changes that last for months to years, the most dramatic and comprehensive molecular rewiring and multicellular re-organization occur in the first few days, which determine the overall progression and prognosis of SCI, yet remain poorly understood. Here, we resolved the spatiotemporal architecture of multicellular gene expression in a mouse model of acute SCI, and revealed the coordinated gene co-expression networks, the upstream regulatory programs, and *in situ* cell-cell interactions that underlay the anatomic disorganization as well as the immune and inflammatory responses conferring the secondary injury. The spatial transcriptomic analysis highlights that the genes and cell types in the white matter (WM) play a more active and predominant role in the early stage of SCI. In particular, we identified a distinct population of WM-originated, *Igfbp2*-expressing reactive astrocytes, which migrated to the grey matter and expressed multiple axon/synapse-supporting molecules that may foster neuron survival and spinal cord recovery in the acute phase. Together, our dataset and analyses not only showcase the spatially-defined molecular features endowing the cell (sub)types with new biological significance but also provide a molecular atlas for disentangling the spatiotemporal organization of the mammalian SCI and advancing the injury management.

45 **MAIN** (*≤2,500 words*):

46 Spinal cord injury (SCI) causes neuronal death, synapse loss, axon retraction, demyelination,
47 inflammation and immune activation, macrophage and immune cell infiltration, gliosis and so
48 forth, which may result in permanent motor, sensory and autonomic dysfunctions
49 accompanied by various local or systemic complications. Both the primary injury and the
50 secondary injury (caused by the initial injury-induced responses) contribute to the overall
51 pathology and disease progression[1-4]. While the chronic phase of SCI can last for months to
52 years, the most dramatic and intensive changes in gene expression and molecular
53 programming take place in the immediate phase (within hours) and the acute phase (a couple
54 of days), followed by the subacute phase (the first two weeks) when secondary injury is
55 triggered and glial scar forms, which leads to further damage to the spinal cord and sets a
56 barrier to axonal regeneration in the chronic phase[1,5,6]. Thus, dissecting the multicellular
57 transcriptional programs and cell-cell communications in the early stage of SCI, in particular
58 the immediate and the acute phases that foretell the injury site re-organization and the overall
59 prognosis, is instrumental to the understanding of SCI pathology and development of new
60 therapeutic strategies.

61 Significant advancements and valuable insights into cell type-specific regulatory
62 programs of gene expression in SCI have been achieved with the advent of single-cell (sc)
63 and single-nucleus (sn) RNA-sequencing (RNA-seq)[7-9]. However, a spatially-resolved view of
64 the changes in the transcriptional landscape and the molecular anatomy of the different spinal
65 cell types as well as their context-dependent injury responses are largely missing, especially
66 for the “enigmatic” early stage of SCI. The recent innovation in spatial transcriptomics, which
67 allows high-throughput measurement of gene expression while retaining the anatomic
68 information[10,11], has been applied to build cell atlases and characterize different biological
69 processes, including normal tissue and organ development, pathological and
70 neurodegenerative diseases[12-21]. Given its value in molecular profiling of physically intact
71 tissue samples in chronic conditions, we made an attempt to employ spatial transcriptomics

72 to investigate traumatically damaged mouse spinal cords in acute injury, aiming to gain a
73 holistic understanding of the intertangled early-phase transcriptional programs and regulatory
74 networks that determine and underlie the SCI-induced molecular and cellular changes in their
75 morphological context.
76

77 **The mouse SCI model and the workflow of the spatial transcriptomic analyses**

78 For the spatial transcriptomic analysis of mammalian SCI in this study, the spinal cord of
79 C57BL/6J mice was fully transected at the tenth thoracic vertebra (T10) (Fig. 1a and Extended
80 Data Fig. 1a). The motor function and the morphology of the spinal cord after injury were
81 examined at 0 (uninjured), 3, 24 and 72 hours post injury (hpi) to confirm a complete
82 transection (Extended Data Fig. 1b-d). We performed hematoxylin and eosin (H&E) staining
83 on transverse sections of various distances from the injury epicenter on both the rostral (-)
84 and caudal (+) segments (Extended Data Fig. 1e). As shown in Extended Data Fig. 1d and e,
85 the spinal cords were severely deformed within ±0.25 mm, precluding an informative spatial
86 transcriptomic analysis. Therefore, the rostral (-) and the caudal (+) sections at ±0.5 and ±1.0
87 mm from the injury epicenter were subjected to the 10x Visium spatial RNA-seq analysis. Four
88 consecutive cryosections each at ±0.5 and ±1.0 mm were captured, and the spinal sections
89 of the same distance at different time points (0, 3, 24 and 72 hpi) were attached to the same
90 Visium Gene Expression slide and processed simultaneously in the subsequent procedure
91 (Fig. 1b). Together, 64 spinal cord sections from 9 different mice were examined in this spatial
92 transcriptomic analysis, representing an inclusive coverage of the dynamic injury responses
93 in a high spatial and temporal resolution.

94 Overall, 22,820 spatial spots were obtained and profiled after filtering, with a mean of
95 12,570 RNA reads and 3,996 genes per spot (Extended Data Fig. 2a-d and Supplemental
96 Table 1). The discernible grey matter (GM) regions containing condensed neuronal cells
97 showed higher numbers of expressed genes (Extended Data Fig. 2d). We compared the intra-
98 and inter-correlations of the sample groups and found a high data reproducibility of the
99 replicate sections within each group at the bulk level (Extended Data Fig. 2e). We therefore

100 analyzed all the sampled spots of the four replicates but visualized the results on each
101 representative sample section in all the spatial view charts in this study.

102 Further spatiotemporal evaluation of the expression of known injury-related genes (e.g.,
103 *Atf3*, *Hmox1* and *Timp1*), aka, the injury score (see Methods), displayed remarkable patterns
104 in association with the injury time, the distance to injury epicenter and the anatomy of the
105 spinal cord (Extended Data Fig. 2f, g). For example, the ±0.5 mm spinal sections at 72 hpi
106 displayed the highest injury scores (Extended Data Fig. 2f, g) and the lowest transcriptomic
107 similarity to others (Extended Data Fig. 2e), which were in accordance with the most severe
108 damage among all the 64 sections (Extended Data Fig. 1e). Therefore, in the subsequent data
109 analyses, we focused on revealing: (1) the spatiotemporal molecular annotation of the spinal
110 cord anatomy, (2) the gene co-expression modules and regulatory networks, and (3) the spinal
111 cell type composition and cell-cell communications in response to SCI (Fig. 1c). For readers
112 with broader research interests, an interactive data exploration portal is available at: *(will*
113 *release to the public upon acceptance of the paper)*.

114

115 **Cluster analysis of the spatial spots reveals anatomic domain- and injury time-featured**
116 **expression profiles of SCI**

117 We first performed dimension reduction and cluster visualization on the collective spatial spots
118 using uniform manifold approximation and projection (UMAP) (see Methods). Seven distinct
119 gene expression clusters were identified (Fig. 1d) and Clusters 1, 2, 6 and 7 showed a bona
120 fide anatomic and molecular annotation of the intact spinal cord at 0 and 3 hpi (Fig. 1e). This
121 allowed us to categorize the seven clusters into four spatial domains according to the four
122 major anatomic regions of the spinal cord: white matter (WM), middle grey (MG), dorsal horn
123 (DH) and ventral horn (VH) (Fig. 1f, g). With the injury score increased along the time
124 (Extended Data Fig. 2f, g), the physical boundary of the anatomic regions became less clear
125 at 72 hpi especially with the ±0.5 mm sections (Fig. 1e). However, the cluster analysis could
126 still classify the spatial spots to the four distinct spatial domains following the coherence in the

127 UMAP plot (Fig. 1g), which showcased the advantage of spatial transcriptomics in providing
128 the molecular annotation of tissue architecture to better understand the SCI pathology.

129 Time after injury, along with the anatomic domain, comprised the major transcriptomic
130 differences amongst the spatial spots of the spinal cord examined in this study (Fig. 1h). In
131 contrast, the rostral/caudal directionality and the distance to the injury site showed mild
132 impacts on distinguishing the clusters (Fig. 1i, j). Consistently, analysis of differentially
133 expressed genes (DEGs) revealed remarkable domain-dependent alterations, whereas only
134 a small number of directionality- or distance-specific DEGs were identified during SCI (except
135 for the ±0.5 mm sections at 72 hpi, where more severe damage was associated) (Extended
136 Data Fig. 3a-c). As such, we focused on the factors of spatial domain and injury time in the
137 subsequent analyses (also see Extended Data Fig. 3d-g).

138 A remarkable shift of the compositions of spatiotemporal clusters in the WM and MG
139 domains was elicited by SCI (Fig. 1k). To understand the molecular changes and functional
140 relevance of these changes, we identified the cluster-enriched genes (CEGs) for each cluster
141 and analyzed their spatiotemporal expression profiles (Fig. 1l). The CEGs included not only
142 the well-known markers of the four anatomic regions of the intact spinal cord, such as *Mbp*
143 (Cluster 1) for WM, *Snap25* (Cluster 2) for MG, *Tac2* (Cluster 6) for DH and *Prph* (Cluster 7)
144 for VH, with their spatial expression validated by *in situ* hybridization (ISH) (Fig. 1m), but also
145 uncharted signature genes for the different spatial domains especially after injury (Extended
146 Data Fig. 4). Gene ontology (GO) term enrichment analyses of the CEGs revealed the
147 biological processes that not only reflect the unique physiological function of the different
148 anatomic regions, but also underlie the pathological progression of SCI. For example, Cluster
149 1 was predominantly localized to the WM at 0 and 3 hpi (Fig. 1k), and its CEGs, such as the
150 myelin-related genes *Plp1*, *Mog* and *Mbp*[22], were enriched in the biological functions of
151 myelination and oligodendrocyte differentiation (Fig. 1l). At 24 and 72 hpi, the main clusters of
152 the WM switched to Clusters 4 and 5 (Fig. 1k), whose CEGs, such as the reactive astrocyte
153 markers *Vim* and *Tm4sf1*[23] in Cluster 4 and the activated macrophage markers *Lyz2* and
154 *Lgals3*[24] in Cluster 5, were enriched with the terms of protein synthesis, cell migration,

155 responses to wounding, *etc*. (Fig. 1l). Thus, the switch of the spatiotemporal clusters in the
156 WM between 3 and 24 hpi suggested a reduction of myelination-related functions along with
157 the activation of astrocytes and infiltration of myeloid cells in the WM regions between the
158 immediate phase and the acute phase of SCI.
159

160 **Spatiotemporal analysis of gene co-expression patterns and transcriptional programs**
161 **in SCI**

162 Next, to depict the intricate and dynamic transcriptional changes in SCI and unveil the
163 commonalities in the molecular events and regulations, we performed the weighted gene co-
164 expression network analysis (WGCNA)[25] (Fig. 2a). Thirty-three spatially and temporally co-
165 expressed gene modules (CGMs) were identified (see Methods and Supplemental Table 2),
166 which displayed unique and diverse spatiotemporal expression patterns, cellular functions,
167 gene connectivity networks and transcriptional regulations (Extended Data Fig. 5 and 6),
168 together providing an unbiased molecular annotation of the injury-induced expression
169 programs in SCI. For example, CGM13 showed an injury-induced expression in the WM
170 specifically at 3 hpi, after which the expression was sharply decreased (Fig. 2b). This module
171 was highly associated with the cellular functions of regulating the ERK1/2 signaling cascade,
172 and the node genes of the connectivity network were *Csrnp1* and *Maff*, which were known
173 players in stress, immune and inflammatory responses[26,27]. Thus, CGM13 likely represented
174 a group of MAPK/ERK-mediated "early response genes" regulating immunity and
175 inflammation in the acute phase of SCI.

176 In addition, we noticed that some modules, such as CGM9 and CGM11, exhibited an
177 interesting spatiotemporally-complementary expression pattern: CGM9 was expressed at a
178 low level in the WM of the intact spinal cord (0 hpi) and at 3 hpi, but was robustly increased at
179 24 hpi, which expanded into the MG in the ±0.5 mm sections at 72 hpi (Fig. 2c). In contrast,
180 CGM11 was highly expressed in the MG at 0 and 3 hpi, which started to decrease at 24 hpi
181 and only retained weak expression at 72 hpi, with the expression in the ±0.5 mm sections
182 reduced the most (Fig. 2d). Scrutinizing the biological functions and the connectivity network

183 of the genes enriched in these two CGMs, we found that CGM9 was mainly involved in stress,
184 wound and immune responses, whereas CGM11 was mostly associated with the function and
185 maintenance of neuronal synapse. Thus, this complementary expression pattern of the two
186 CGMs likely underscored the interplay of SCI-induced immunity and inflammation with the
187 loss of neurons and synapses during SCI.

188 To further unravel the regulatory mechanisms that determine the spatiotemporal changes
189 in gene expression in SCI, we performed single-cell regulatory network inference and
190 clustering (SCENIC) analysis[28] to identify transcriptional regulons (consisting of the
191 transcription factors (TFs) and their target genes) that could coordinately regulate gene
192 expression in response to SCI. Overall, 147 regulons were identified and classified into seven
193 regulon modules (RMs) (Fig. 2e and Supplemental Table 3). The RMs showed remarkable
194 anatomic domain- and/or injury time-specificity (Fig. 2f and Extended Data Fig. 7). For
195 example, RM4 and RM7 functioned predominantly in the DH and the VH, respectively; RM6
196 was enriched in the GM regions including MG, DH and VH and its activity was gradually
197 reduced along the time in SCI; RM5 was highly expressed in the DH and the WM at 3 hpi,
198 which may be associated with the induction of the early response genes.

199 The RMs of the WM were more complicated and dynamic: RM2 was the main RM at 0
200 and 3 hpi, and it was superseded by RM3 at 3 and 24 hpi and finally by RM1 at 72 hpi (Fig.
201 2f, g and Extended Data Fig. 7a, b). Along with these changes, the TFs of the main regulons
202 in the WM switched from Sox10, Oligo2 and Srebf2 (RM2), to Fos, Jun and Nfkb1/2 (RM3),
203 and ultimately to Stat3, Stat6 and Irf5 (RM1) (Fig. 2h). Sox10 and Oligo2 are important TFs in
204 oligodendrocyte differentiation and maturation[29] and Srebf2 regulates genes involved in
205 cholesterol biosynthesis[30]; Fos and Jun are key TFs in TGFβ-mediated signaling and regulate
206 cell proliferation, differentiation and death[31] and Nfkb1/2 is a central activator of genes related
207 to inflammation and immune functions[32]; Stat3, Stat6 and Irf5 mediate gene expression in
208 response to cell stimuli and are widely involved in immunity, inflammation and cell death[33].
209 Together, the shifts of the main RMs in the WM (Fig. 2f) were in agreement with the changes
210 of the spatiotemporal clusters in the WM during SCI (Fig. 1k), which underscored the injury-

211 induced oligodendrocyte dysfunction and immune and inflammation activation in the WM. Of
212 note, the immune and inflammatory responses mediated by RM3 at 3 and 24 hpi were largely
213 restricted to the WM, whereas those by RM1 at 72 hpi were comparably activated in all the
214 four anatomic domains (Fig. 2f and Extended Data Fig. 7a), suggesting a widespread
215 upregulation of immune and inflammatory genes by the end of the acute phase of SCI.
216

217 **Integration of the SCI scRNA-seq data for an *in situ* multicellular gene expression and**
218 **cell communication atlas**

219 Because the Visium spot is not single-cell resolution, to allocate the cell type information to
220 the SCI spatial spots in a comparable manner, we performed deconvolution analysis by robust
221 cell type decomposition (RCTD[34]; also see Methods) using the combined normal and injured
222 spinal cord scRNA-seq datasets as reference[9,35]. The proportions of different cell types
223 detected within a single spatial spot were displayed as a pie chart and the entire spinal cord
224 section was displayed as an assembly of the spatial pie charts (Fig. 3a, b). The overall
225 composition of the main cell types and their anatomic localizations were in good accordance
226 with the spatial architecture of the spinal cord. For example, neurons and oligodendrocytes
227 were predominantly localized to the GM and the WM, respectively (Fig. 3b). Interestingly, we
228 found that the two molecularly-defined astrocyte subtypes, astrocyte-*Gfap* and astrocyte-
229 *Slc7a10*[35] (Supplemental Table 4), showed distinct and mutually exclusive distributions in the
230 white (namely, astrocyte-WM) and grey matter (namely, astrocyte-GM), respectively (Fig. 3b),
231 which represented the general categories of astrocyte heterogeneity in location of white
232 (fibrous astrocyte) versus grey matter (protoplasmic astrocyte)[36]. Furthermore, deciphering *in*
233 *situ* spinal cell type compositions and their spatiotemporal dynamics during SCI revealed
234 sophisticated spatial domain- and injury time-associated alterations (Extended Data Fig. 8),
235 including the emergence of the cell types that participate in the scar formation such as
236 fibroblasts, ependymal and vascular cells as well as the invasion of peripheral immune and
237 inflammatory cell types such as myeloid cells, macrophages, monocytes and neutrophils (Fig.
238 3c and Extended Data Fig. 9).

239 Cell-cell interaction plays important roles in maintaining tissue integrity and normal
240 functions. To denote faithful *in situ* cell-cell interactions from our spatial transcriptomic data,
241 we performed a spatial-aware cell-cell communication (SA-CCC) analysis. In brief, spatial
242 colocalization of cell-type pairs within spots and spot-enriched ligand_receptor (L_R) pairs
243 deduced from CellChat package[37] were subjected to co-occurrence test (Fig. 3d and see
244 Methods). Upon injury, both the number of interacting L_R pairs per cell-type pair and the
245 complexity of the network of co-localized cell types were markedly increased, especially at 72
246 hpi (Fig. 3e). Among all the cell types, oligodendrocytes and astrocytes had the most extensive
247 connections and served as the nodes to interact with other cell types in both intact and injured
248 spinal cords, especially at 72 hpi. In addition, the connectivity of macrophages, reactive
249 microglia, OPCs and fibroblasts was substantially increased, indicating much escalated
250 diversity of cell-cell communications in this stage of SCI.

251 To pinpoint the specific L_R pairs that mediate the spatiotemporal dynamics of cell-cell
252 communications, the top L_R pairs in each cell-type pair at different time points in SCI were
253 identified and examined (Extended Data Fig. 10a) and three main classes of L_R pairs were
254 discerned (Extended Data Fig. 10b). Unlike the cell-cell communication analysis based solely
255 on scRNA-seq datasets, the SA-CCC analysis is featured by identifying both the expression
256 levels and the *in situ* interacting cell types for a particular L_R pair in a context-dependent
257 manner. For example, the L_R pair of *Spp1_Cd44* was expressed predominantly in the WM
258 at moderate levels at 0 and 3 hpi, which was increased remarkably at 24 hpi (primarily in the
259 WM and scattered in some GM regions) and spread throughout the entire spinal cord section
260 at 72 hpi (Extended Data Fig. 10c). Accompanying this profound induction, the interactions of
261 the cell-type pair(s) mediated by the L_R pair of *Spp1_Cd44* expanded from
262 “oligodendrocyte_astrocyte-WM” to “astrocyte-WM_OPC” in the WM at 24 hpi and finally to
263 “oligodendrocyte_macrophage” and “OPC_macrophage” in the GM at 72 hpi (Extended Data
264 Fig. 10c), suggesting a multifaceted role of this L_R pair along the progression of SCI.
265

266 **Injury induces redistribution and repurposing of astrocytes-WM into the GM of the**
267 **spinal cord**

268 Astrocytes are morphologically and functionally diverse and play vital roles in the nervous
269 system in both physiological and pathological conditions[38]. Being a significant portion in the
270 spinal cord, not only the proportions of the two main astrocyte subtypes (WM and GM) altered
271 dramatically (Fig. 3c), but also their weights in coordinating cell-cell communications in SCI
272 differed a lot (Fig. 3e). Indeed, the gene expression features, GO term analysis of the DEGs
273 and their upstream transcriptional regulons as well as cross-reference with two single-cell SCI
274 datasets all pointed to the molecular basis underlying their spatial and functional divergences
275 (Extended Data Fig. 11). Thus, our spatial classification of astrocytes-WM and astrocytes-GM
276 corroborates the different physiological functions of the known astrocyte subtypes in the
277 mammalian nervous system[39,40].

278 Strikingly, the two astrocyte subtypes displayed quite different injury-induced changes in
279 their spatiotemporal distributions in response to SCI: astrocytes-WM were largely unchanged
280 at 3 hpi but were drastically increased at 24 and 72 hpi, at which they were even present in
281 the GM region; astrocytes-GM were increased at 3 hpi but then drastically decreased at 24
282 hpi and became almost undetectable at 72 hpi (Fig. 3f, h). The dynamic changes of distribution
283 were validated by examining the spatiotemporal expression patterns of two representative
284 marker genes (*Gfap* and *Pla2g7*; see Extended Data Fig. 11e) by ISH (Fig. 3g, i). Furthermore,
285 by the SA-CCC analysis of cell-cell interactions in the GM and the L_R pairs mediating these
286 interactions (e.g., the *Nrxn_Nlgn* families) (Fig. 3j), we revealed a clear switch of neuron-
287 interacting cells from “astrocytes-GM” at 0 and 3 hpi to “astrocytes-WM” at 24 and 72 hpi,
288 accompanied by the synchronized switch of the spatial L_R pairs (e.g., *Nrxn3_Nlgn3*) (Fig.
289 3k). The *Nrxn3_Nlgn3* is well known for regulating astrocyte maturation as well as synapse
290 development and function[41]. Thus, these findings strongly suggested a functional relay of the
291 original astrocytes-GM to GM-relocated astrocytes-WM at the end of the acute phase of SCI.

292 To further confirm the injury-induced relocation of astrocytes-WM to the GM at 72 hpi, we
293 performed immunostaining of the spinal astrocytes with anti-GFAP. The results not only

294 verified the predominant localization and fibrous appearance of GFAP$^+$-astrocytes in the WM
295 of the intact and injured spinal cord but also showed a remarkable emergence of GFAP$^+$-
296 astrocytes in the GM after injury, and these GM-relocated GFAP$^+$-astrocytes displayed a
297 hypertrophic morphology (Fig. 3l). The loss of astrocytes-GM at 24 and 72 hpi and the striking
298 occupation of massive GFAP$^+$-astrocytes in the GM prompted us to further investigate the
299 molecular origin and the potential functions of these GM-relocated astrocytes. To avoid
300 confusion due to the discrepancy in the anatomic localization and the transcriptional features,
301 we designated the injury-induced, GM-relocated astrocytes as "astrocytes-GMii" in the
302 subsequent study.
303

304 **The astrocytes-GMii are molecularly distinct from the original astrocytes-WM/-GM and**
305 **may contribute to spinal cord rescue/repair**

306 We were keen to know where these astrocytes-GMii came from and what function(s) they
307 played in the GM. Toward this end, we performed a series of exploratory data analyses and
308 also cross-tested with the published scRNA-seq datasets of mouse SCI (Fig. 4a). As an
309 attempt to address the question whether astrocytes-GMii were derived from local cell division
310 or remote cell migration, we calculated and compared the proliferation score and the migration
311 score (see Methods) at the spatial and cell type levels (Fig. 4b-e and Extended Data Fig. 12a,
312 b). The results showed that significant cell proliferation was detected in the spots enriched by
313 astrocytes-WM, reactive microglia and other cell types only at 72 hpi, much later than the time
314 when a large number of astrocytes-GMii emerged. In contrast, the migration score started to
315 increase in astrocytes-WM as early as 3 hpi, which kept rising at 24 hpi and expanded into the
316 GM at 72 hpi. Notably, astrocytes-GM persistently showed the low proliferation and migration
317 scores with a minimal increase of migration at 3 hpi. In addition, our analysis of the SCI
318 scRNA-seq dataset[9] also indicated a markedly higher migration ability associated with
319 astrocytes-WM than astrocytes-GM (Extended Data Fig. 12b). Together, astrocytes-GMii
320 likely originated from astrocytes-WM, which migrated into the GM and proliferated to
321 compensate for the loss of original astrocytes-GM in the acute phase of SCI.

322 To reveal what unique molecular features astrocytes-GMii possess that made these cells
323 distinct from the other astrocytes-WM and drove them into the GM upon injury, we assessed
324 all the spots containing astrocytes-WM (astrocyte-WM spots) in our spatial transcriptomic
325 dataset (Fig. 4f) using the anatomical definition by aforementioned UMAP clustering (Fig. 1g,
326 k). In addition, to exclude potential confounding influences from other cell types in the same
327 spot, only the 317 astrocyte marker genes used for cell type deconvolution were included.
328 Despite considerable overlapping in their expression features that contribute to the general
329 identity of astrocytes, these 317 marker genes could be clustered into four spatiotemporally-
330 distinct astrocyte (SA) groups (Fig. 4g and Supplemental Table 5). Among them, the SA-1
331 group showed specifically high expression in the GM region at 24 and 72 hpi, while the SA-4
332 group also showed increased expression in the GM after injury, albeit to a lesser extent. We
333 speculated that a SA score computed by these two SA gene sets would serve to spatially
334 define the molecular features of astrocyte-GMii. Interestingly, the SA score was positively
335 correlated with the proportion of remaining neurons in the spatial spots at 72 hpi (Fig. 4h, i).
336 Together with the earlier SA-CCC analysis indicating a functional relay of astrocytes-GM to
337 astrocytes-GMii at the end of the acute phase of SCI (Fig. 3j, k), these data suggested that
338 the emergence of astrocytes-GMii and their interaction with neurons likely compensated for
339 the loss of original astrocytes-GM and provided structural and nutritional support to the
340 neurons spared from the primary injury.

341 To test the utility of the SA score for distinguishing astrocytes-GMii from the general
342 population of astrocytes-WM in other spinal cord studies, we re-clustered the astrocytes-*Gfap*
343 in the SCI scRNA-seq dataset[9]. Indeed, these cells were gated into two distinct populations
344 based on the SA scores: astrocytes-GMii and the rest astrocytes-WM (-WMrs) (Extended Data
345 Fig. 12c), which were also separated from each other in the UMAP plot (Fig. 4j). Next, to
346 expand the spatially-defined molecular features of astrocytes-GMii, we identified the signature
347 genes of astrocytes-GMii and -WMrs in the whole injured single-cell dataset (Extended Data
348 Fig. 12d). Also, to facilitate precise sorting and genetic manipulation of astrocytes-GMii in the
349 future, we further examined the potential surface markers and the upstream TFs of astrocytes-

350 WMrs, -GMii and -GM (Extended Data Fig. 12e, f). It was worth noting that astrocytes-GMii
351 were strongly associated with the increased activity of the Irf and Stat families of TFs, pointing
352 to an immune-triggered transition of astrocytes-WM to astrocytes-GMii. Thus, the findings
353 based on the spatially defined molecular features together the expanded signature genes of
354 astrocytes-GMii demonstrated that our spatial transcriptomic analysis could provide valuable
355 metrics to annotate independent cell states that are often hidden in common single-cell
356 approaches.

357 To elucidate the molecular programming driving the transition of the original astrocytes-
358 WM to the SCI-induced astrocytes-GMii, we performed pseudo-trajectory analysis of the SCI
359 single-cell dataset by slingshot[42]. We identified continuous transitive structures between
360 associated clusters in the low dimensional data (Fig. 4j, k) and highlighted the most
361 dramatically altered genes along this transition (Fig. 4l). One of such genes was *Igfbp2*
362 (*insulin-like growth factor binding protein 2*), and fluorescence ISH (FISH) of *Igfbp2* together
363 with immunostaining of GFAP confirmed that astrocytes-GMii, represented by the *Igfbp2*$^{+}$-
364 GFAP^{+} double-positive cells, were specifically induced in the GM of injured spinal cord
365 especially at 72 hpi (Fig. 4m). *Igfbp2* is a developmentally regulated gene that is highly
366 expressed in the developing brain and markedly decreases after birth[43,44], while its aberrant
367 expression in cancer has been proposed to act as a hub of the oncogenic network that
368 promotes tumor growth and metastasis[44,45]. Here, we showed that overexpression (OE) of
369 *Igfbp2* in primary cultures of mouse astrocytes by lentiviral infection significantly promoted
370 astrocyte migration in the *in vitro* scratch assay (Fig. 4n). Thus, the expression of *Igfbp2* not
371 only can serve as a molecular marker for astrocytes-GMii but may also underlie the migration
372 of astrocytes-WM to the GM in response to SCI.

373 Finally, to explicate the biological significance of astrocytes-GMii, we compared the
374 DEGs and their enriched GO terms of astrocytes-WMrs, -GMii and -GM in the SCI single-cell
375 dataset (Fig. 4o and Supplemental Table 6). The results indicated that astrocytes-GMii shared
376 several neurotrophic functions in common with astrocytes-GM, which once again suggested
377 a functional replacement of astrocytes-GM by astrocytes-GMii. In addition, the astrocyte-GMii

signature genes such as *Vegfa*, *Gpr37l1*, *Fgfr3* and *Fgfr1* were associated with a protective role in neurological disorders[46], which was consistent with the outcome of better neuronal survival observed in the higher SA scores of astrocytes-GMii (Fig. 4h, i). Together, as both the previous[47] and this study showed that migrating astrocytes together with other cells in the SCI lesions expressed multiple axon/synapse-growth-supporting molecules, we anticipate that the surge of *Igfbp2*$^{+}$-astrocytes to the GM of the injured spinal cord may provide neurotrophic support for spare neuron survival and spinal cord rescue in the acute phase of SCI (Fig. 4p). Future investigation is warranted for the finer classification of astrocytes-GMii and understanding of their spatial features and functional implications.

387 **Discussion**

388 The spinal cord is a highly structured organ composed of various cell types that are well
389 organized to perform complicated yet interdependent physiological functions. Two earlier
390 spatial transcriptomic studies of the mammalian spinal cord identified pathway dynamics
391 during the disease progression of ALS[13] and described various cell transcriptional states over
392 the course of injury-induced scar formation[48]. Meanwhile, several single-cell studies have
393 demonstrated complex cellular heterogeneity and interactions in the mouse spinal cord[9,35,49-
394 52]. How the diverse cell types respond and crosstalk to one another in a spatial- and context-
395 dependent manner, especially in the early stage of SCI, drives the subsequent pathological
396 process and is central to the pathophysiology of SCI. Here, we implemented the spatial
397 transcriptomics to characterize the spatiotemporal programming of gene expression and cell
398 organization in the immediate and the acute phase of SCI. We characterized and analyzed
399 the spatiotemporal changes in gene expression, TF activities, regulon networks, cell
400 compositions as well as cell-cell communications in SCI. To demonstrate the utility of the rich
401 information generated in this study, we have set up an interactive web-portal for other
402 researchers to explore *in situ* gene expression dynamics in SCI *(will release to the public upon*
403 *acceptance of the paper)*.

404 Glial cells in the WM are generally considered to provide support and maintain
405 extracellular homeostasis to neurons, forming myelin and clearing debris. Interestingly, our
406 spatiotemporal transcriptomic data indicate that genes and cells in the WM respond to SCI
407 more rapidly, robustly and sophisticatedly than those in the GM. The main molecular features
408 of the WM shifted twice from Cluster 1 to 4 and then to 5, whereas the GM changed only once
409 from Cluster 2 to 3 (Fig. 1). Moreover, the early response gene modules (e.g., CGM13 and
410 CGM22), involving the MAPK/ERK signaling cascade, cytokine production and other immune
411 and inflammatory responses, were activated in the immediate phase at 3 hpi in the WM but
412 not the GM (Fig. 2). Thus, the glial cells in the WM do not merely insulate axons or respond

413 subordinately to neuronal damage. Rather, they behave as the “first responders” in SCI and
414 play a more active, leading and probably decisive role than previously thought.

415 SCI triggers multicellular gene expression changes in a temporally and spatially
416 coordinated manner. When characterizing cell type-specific responses and cell-cell
417 communications, single cell-based analyses are limited by the sampling bias in the tissue
418 dissociation procedure and low-coverage sequencing[53]. To amend this, we took the
419 advantage of spatial transcriptomics and developed a new computation strategy (SA-CCC) to
420 unfold the cell communication by simultaneous evaluation of the physical distance between
421 any cell-type pair and the locally aggregated expression level of a L_R pair that is supposed
422 to express in this cell-type pair (Fig. 3). Using this approach, we not only systematically
423 illustrate an overview of *in situ* cell-cell interactions of SCI, but also provide a useful toolset for
424 evaluation of intercellular communications in a comprehensive multicellular context in
425 biological processes and diseases.

426 Astrocytes are dynamic, diverse cells whose molecular and functional heterogeneity is
427 closely related with the local environment[54,55]. Despite their being a barrier to axonal
428 regeneration in the later phases, migrating reactive astrocytes that form the glial scar play a
429 beneficial role by the closure of the wound and segregation of immune/inflammatory cells,
430 which contribute to the spontaneous, partial functional recovery in the subacute phase[56,57].
431 And, cell-based treatments including the induction of differentiation and migration of reactive
432 astrocytes have emerged as a potential therapeutic strategy to improve the functional recovery
433 in patients[58-61]. However, the specific dynamics and the regulatory programs of astrocyte
434 migration in SCI are still poorly understood, largely due to the difficulty in exploring these
435 mechanisms *in vivo*. In this study, by leveraging the spatiotemporal transcriptomic allocation
436 and profiling different cell types and subtypes, we uncover a distinct population of injury-
437 induced reactive astrocytes (astrocytes-GMii) and explicitly show that these astrocytes
438 originate from the WM and migrate to the GM, in which they interact with spare neurons and
439 other cell types at 24 and 72 hpi. Thus, unlike the double-edged scar-forming astrocytes and
440 those promote detrimental secondary inflammation and immune responses in the subacute

441 and the intermediate phases, this population of astrocytes-GMii respond much rapidly in SCI
442 and function as a hub of the multicellular communication and re-organization in the acute
443 phase, which may support neuronal survival and spinal cord rescue after the primary injury.
444 In addition, the pseudotime trajectory and the DEG analysis strongly suggested that the local
445 environment of the GM triggered the transition of the relocated astrocytes-WM to astrocytes-
446 GMii, and the latter shared certain gene expression similarity with the original astrocytes-GM,
447 especially regarding the neurotrophic function in maintaining neuronal synapses.
448 Nevertheless, these astrocytes-GMii do not necessarily migrate from the same segmental
449 level of the injured spinal cord[62] and are unlikely through tangential astrocyte migration that is
450 absent in adult spinal cord even after injury[63].

451 Astrocytic scars have been studied for several decades; however, the exact molecular
452 mechanisms regulating their formation are not fully understood. This is in part due to the lack
453 of individual markers for the diverse range of subtype- and context-specific astrocytes. For
454 example, in this study, GFAP is strongly expressed in both the original astrocytes-WM and the
455 SCI-induced astrocytes-GMii, despite that their spatial distributions, morphologies, molecular
456 features and cellular functions are quite different. By a series of integrated spatial and single-
457 cell transcriptomic analyses, we not only demonstrate that astrocytes-GMii are molecularly
458 distinct from the original astrocytes-WM and -GM but also identify that these astrocytes-GMii
459 express both the reactive astrocyte marker GFAP and the IGF signaling factor IGFBP2, and
460 the latter may underlie the SCI-induced migration of astrocytes-WM to the GM. Hence, our
461 work exemplifies how the spatiotemporal transcriptomic signatures combined with single-cell
462 resolution may facilitate subtype annotation and functional interrogation in SCI as well as other
463 physiological and pathological conditions. In addition, although the secreted protein Igfbp2
464 was believed to play an essential role in promoting neurite outgrowth in developing and injured
465 brains[64,65], a recent study showed that blocking Igfbp2 in the astrocyte-conditioned medium
466 derived from a Rett syndrome model induced a significant increase in neurite outgrowth[66].
467 Thus, future efforts are warranted to understand the specific role of the increased expression

468 *Igfbp2* in these astrocytes-GMii and to induce the astrocytes-GMii to adopt a neuroprotective
469 and pro-regenerative state that may aid spinal cord repair.

470 Taken together, our work here provides the most comprehensive gene expression
471 profiling of SCI (to the best of our knowledge), involving injury time, distance, directionality,
472 anatomic domain, cell type and other dimensions. As summarized in Extended Data Fig. 13,
473 this study disentangles the SCI-induced complex transcriptional programs and multicellular
474 responses in the tissue context and establishes a spatiotemporal transcriptomic landscape for
475 in-depth research in the future, providing an open data resource and a platform for identifying
476 potential targets for therapeutic intervention of SCI.

477 **FIGURE LEGENDS** *(< 250 words each)*

478 **Fig. 1. Spatiotemporal transcriptomics and molecular clusters of mouse SCI using**
479 **Visium**

480 (**a**) A carton of the mouse SCI model and the spinal cord sections obtained in this spatial
481 transcriptomic study. (**b**) A schematic of the Visium Gene Expression slide and the acquisition
482 of the mouse SCI sections for RNA-sequencing. (**c**) The main workflow of the spatial
483 transcriptomic data analyses. (**d**) The UMAP plot of the 22,820 transcriptomic profiles (one
484 profile for each spatial spot) of all the SCI samples identified 7 spatiotemporal clusters. (**e**)
485 The clusters are color coded and shown in the spatial view of the spinal cord sections at the
486 indicated locations and time points after injury. (**f**) A cartoon showing the main anatomic
487 regions of the spinal cord: WM, white matter; MG, middle grey; DH, dorsal horn; VH, ventral
488 horn. (**g-j**) The UMAP plots of the spatial spots were colored according to anatomic region (**g**),
489 time after injury (**h**), directionality (**i**) and distance to the injury site (**j**). (**k**) Quantification of the
490 numbers of the spatial spots in each cluster at the indicated time points. (**l**) The heatmap
491 showing the expression levels of the top 10 CEGs (left) and the dot-plot showing the top 5 GO
492 terms (right) for each of the 7 spatiotemporal clusters. (**m**) The spatial view of the gene
493 expression levels in the spatiotemporal transcriptomics (ST, left) and *in situ* hybridization (ISH,
494 right) of four representative anatomic markers as indicated. Scale bar: 500 μm. SCI, spinal
495 cord injury; hpi: hours post injury; UMI, unique molecular identifier; UMAP, uniform manifold
496 approximation and projection; CEGs, cluster-enriched genes; GO terms, gene ontology terms;
497 *p*. adjust, adjusted *p* value.

498

499 **Fig. 2. Spatiotemporal analyses of gene co-expression dynamics and regulatory**
500 **networks in SCI**

501 (**a**) Heatmap showing the weighted-correlation network of the genes constituting 33 SCI
502 spatiotemporal CGMs. (**b-d**) The molecular features of three representative CGMs: CGM13
503 (**b**), CGM9 (**c**) and CGM11 (**d**). From left to right: Left, the spatial view of average levels of the

genes expressed in the indicated CGM during the process of SCI; middle, the ridge plot quantitatively illustrating the density distribution of the CGM expression within the 4 anatomic domains at the indicated time points of SCI; right, the representative GO terms (top) and the gene network showing the highest 50 connectivity weights (bottom) of the indicated CGM. The number of genes in each CGM is shown in the parentheses. (**e**) The CSI heatmap of 147 transcriptional regulons grouped into 7 RMs by hierarchical clustering. (**f**) The heatmap of the overall activity of each RM enriched in the four anatomic domains at the indicated time points of SCI. (**g**) The spatial view of the average regulon activity of RM2 at the indicated time points of SCI. The number of regulons in RM2 is shown in the parentheses. (**h**) The Pearson correlation networks and the CSI connectivity degree of the transcriptional regulons within and across the 7 RMs. CGM, co-expressed gene module; CSI, connectivity specificity index; RM, regulon module.

Fig. 3. Analyses of multicellular responses and cell-cell communications in SCI identify injury-induced, GM-relocated astrocytes-WM

(**a, b**) The spatial views of the spots showing the proportions of all cell types in each spot (as a pie chart) of the spinal sections at the indicated time points in SCI (**a**), and the zoom-in of the yellow-boxed area with the spatial distributions of the representative spinal cord cell types is shown in (**b**); also see Extended Data Fig. 7-8. (**c**) The fractions (%) of different cell types at indicated time points in SCI. (**d**) A schematic cartoon illustrating the main procedure for the spatial-aware cell-cell communication (SA-CCC) analysis that evaluates *in situ* intercellular communications by testing the statistical significance of the co-occurrence of a cell-type pair and an L_R pair. (**e**) The SA-CCC networks at each indicated time point in SCI. The size of the orange circles represents the number of the interacting L_R pairs expressed in each cell-type pair. For the connecting lines, the thickness denotes the GeoM of the significance of the interaction and the shade indicates the average expression levels of the L_R pairs for each cell-type pair. (**f-i**) The spatiotemporal distributions of astrocytes-WM (**f**) and astrocytes-GM (**h**), validated with ISH of *Gfap* for astrocytes-WM (**g**) and *Pla2g7* for astrocytes-GM (**i**). Scale

532 bars: 500 μm. (**j**) Dot plots showing the major interacting L_R pairs of the main cell-type pairs
533 in the GM at the indicated time points in SCI (from Extended Data Fig. 10a). (**k**) From left to
534 right: left, the geometric proportions of the cell-type pairs of "astrocyte-GM_neuron" and
535 "astrocyte-WM_neuron"; middle, the expression levels of the individual ligand, receptor, and
536 their geometric mean of the L_R pair of *Nrxn3_Nlgn3*; right, the average expression of the
537 *Nrxn3_Nlgn3* pair within the indicated co-localized cell-type pairs along the time in SCI. (**l**)
538 Immunostaining of GFAP in the mouse spinal cord (-1.0 mm section) at 0 and 72 hpi. The
539 morphologies of $GFAP^+$-astrocytes in the GM (yellow box) and the WM (cyan box) are shown
540 in the zoom-ins on the right. Scale bars: 200 μm (left) and 20 μm (right). Astro, astrocytes;
541 WM, white matter; GM, grey matter; H-Microglia, homeostatic microglia; R-Microglia, reactive
542 microglia; GeoM, geometric mean; EM, assembly mean; L_R pair, ligand_receptor pair; ISH,
543 *in situ* hybridization.
544
545 **Fig. 4. Characterization of the molecular features of SCI-induced astrocytes-GMii with**
546 **spatial transcriptomics and scRNA-seq integration**
547 (**a**) An overview of the comprehensive spatial and single-cell transcriptomic analyses (in Fig.
548 4 and Extended Data Fig. 12) for the identification and characterization of the SCI-induced
549 astrocytes-GMii. (**b, c**) The spatiotemporal dynamics of the proliferation (**b**) and migration (**c**)
550 scores in SCI. (**d, e**) The jaccard similarity (JC index) of the proliferation score (**d**) or migration
551 score (**e**) for the spatial spots containing the specified individual cell types at the indicated time
552 points in SCI. (**f**) An example of the spinal cord section showing the H&E staining, the spatially-
553 defined (sd) WM and sdGM domains (annotated using the spatial clusters in Fig. 1g, k), and
554 the spatial spots containing astrocytes-WM. (**g**) The 317 astrocyte deconvolution marker
555 genes in the spatial spots containing astrocytes-WM are clustered into four SA groups based
556 on their bulk expression levels according to the sdWM or sdGM domain and the injury time.
557 (**h, i**) The spatial distributions of the sdWM and sdGM domains, the SA score and neuron
558 proportion in each spot at 72 hpi (**h**) and their scatterplot along the distance (-1.0 to +1.0 mm)
559 as well as the corresponding locally weighted regression fitting curves (**i**) are shown. The

560 normalized values are the z-score [0, 1] of the SA scores and neuron proportions. The
561 Spearman rank correlation coefficient of the SA score and neuron proportion is shown in the
562 paratheses. (**j, k**) The UMAP re-clustering (**j**) and pseudotime trajectory (**k**) analyses of the
563 astrocytes-*Gfap* in the SCI single-cell dataset[9] identify distinct populations of astrocytes-WMrs
564 and astrocytes-GMii sharing a continuous cell lineage. (**l**) The expression heatmap of the top
565 50 most dramatically-altered genes along the trajectory in (k). Among them, an example of
566 *Igfbp2* is examined by FISH in (m). (**m**) Representative confocal images of immunostaining of
567 GFAP combined with FISH of *Igfbp2* of the mouse spinal cord (-1.0 mm section) at the
568 indicated time points in SCI. The white-boxed areas are shown in a higher magnification in the
569 zoom-ins and the 3D rendering of a "GFAP$^+$-*Igfbp2*$^+$" cell at 72 hpi (yellow box) is shown, with
570 DAPI staining to indicate the location of the nucleus. The average densities of the indicated
571 immunophenotypes of cells in the mouse spinal cord area and the percentage of "GFAP$^+$-
572 *Igfbp2*$^+$" cells to total cell counts (indicated by DAPI) at the specified time points in SCI are
573 quantified. Scale bars: 10 μm in 3D rendering, 25 μm in zoom-ins, and 200 μm in the rest. (**n**)
574 Representative brightfield images of the scratch assay of *in vitro* cultured mouse primary
575 astrocytes infected with pCDH-vector (control) or pCDH-*Igfbp2*. The gap (cell-free area)
576 caused by the scratch in multiple random visions of two pooled repeats were traced along time
577 and the average size of the gap was calculated and shown on the right. Scale bar, 100 μm.
578 Mean ± SEM; n = 6; *$p < 0.05$ and ***$p < 0.001$; one-way ANOVA in (m) and Student's t-test
579 in (n). (**o**) GO term analysis of the unique and shared DEGs (left) and the heatmap showing
580 the average normalized expression levels of the DEGs (right) associated with astrocytes-
581 WMrs, -GMii and -GM. The DEGs that are cross-referenced as pro-inflammatory (red),
582 neurotrophic (green) or neuroprotective (in bold) genes by Kaufmann et al.[46] are highlighted.
583 (**p**) A schematic of the SCI-induced, *Igfbp2*-expressing astrocytes-GMii, which originate from
584 reactive astrocytes in the WM and migrate into the GM to provide support to spare neurons.
585 Astro, astrocytes; WM, white matter; GM, grey matter; Astro-GMii, injury-induced GM-
586 relocated astrocytes; Astro-WMrs, the rest astrocytes-WM; SA, spatiotemporally-distinct
587 astrocyte; FISH, fluorescence ISH; hps, hour post scratch.

588 **METHODS** *(< 3,000 words)*

589 **Animal Care**

590 All practices on mice in this study were performed in compliance with the institutional
591 guidelines on the scientific use of living animals at the Shanghai Interdisciplinary Research
592 Center on Biology and Chemistry, the Chinese Academy of Sciences (CAS). Animal distress
593 and conditions requiring euthanasia were addressed and the number of animals used was
594 minimized. All mice were housed in a pathogen-free barrier facility with free access to food
595 and water.

596

597 **Mouse spinal cord injury (SCI)**

598 The C57BL/6J mice (Jackson Laboratory, #000664) used in this study were purchased from
599 the Shanghai Laboratory Animal Center (SLAC). Adult female mice of 8-9 weeks old were
600 used in the SCI. The spinal cord transection was performed as previously described[67]. Briefly,
601 after exposure and removal of the lamina of the tenth thoracic vertebra (T10) spinal segment,
602 the spinal cord was transected with Micro Scissors, and the wound was then cleaned and
603 sutured. For sham controls, only laminectomy at T10 was performed. For post-operative care,
604 the mice received analgesics at the wound every 12 h and were subjected to manual bladder-
605 emptying at least twice daily.

606

607 **Behavioral evaluation of SCI**

608 All animals were accommodated to the testing room or apparatus for at least 1 h before
609 behavioral assessments. Blind scoring was performed to ensure that observers were unaware
610 of treatments. The animals were evaluated for the hindlimb locomotion performance at 0
611 (uninjured), 3, 24 and 72 hours post injury (hpi) by the Basso mouse scale (BMS)[68]. Briefly,
612 mice were placed in an open field for 4 min. Two observers assessed the performance
613 independently with the reference to the motion attributes of the hindlimbs, including joint
614 movement, weight support, plantar stepping, coordination, paw position, and trunk and tail

615 control. The BMS scores range from 0 to 9 points (0 means complete paralysis and 9 means
616 normal mobility). For the mechanical sensitivity (von Frey) test[69], the mice were placed on the
617 bottom of a metal grid and the mid-plantar surface of the hindpaw of the mice was stimulated
618 with 2 g von Frey filaments vertically. The filaments were applied to the hindpaw surface until
619 the filament bent, and paw withdrawal or flinching was considered as a positive response. The
620 test of tactile withdrawal threshold was repeated 10 times in each mouse. The mean value of
621 the performance of the left and right hindlimbs was calculated and used in the BMS and von
622 Frey tests.
623

624 **Cryosection and immunohistochemistry**

625 Anesthetized mice were fixed via transcardial perfusion with diethylpyrocarbonate-treated
626 phosphate-buffered saline (PBS) followed by 4% (w/v) paraformaldehyde (PFA, RNase-free;
627 Bioss, C2055). Spinal cord tissues were then dissected and post-fixed in 4% PFA at 4°C
628 overnight. The fixed spinal cord samples were cryoprotected in 30% (w/v) sucrose (Sangon,
629 A0498) in PBS, embedded in Tissue-Tek O.C.T. (Sakura, 4583), snap-frozen in liquid nitrogen,
630 and stored at -80°C until cryosection. Before cryosection, samples were equilibrated to -20°C
631 in the cryostat for at least 30 min. Cross sections (20 μm) of the spinal cord were collected on
632 the slides and could be stored at -80°C up to 2 weeks.

633 For hematoxylin and eosin (H&E) staining, the spinal cord sections on the slides were
634 incubated at 37 °C for 1 min, and then completely immersed in the prechilled methanol at -
635 20 °C for 30 min. After three washes with deionized water (diH_2O), isopropanol was added to
636 fix the tissue slides at room temperature (RT) for 1 min. Thereafter, the slides were air-dried
637 and hematoxylin (Agilent, S330930-2) was added to the slides at RT for 7 min. After three
638 washes with diH_2O, slides were treated by Bluing Buffer (Agilent, CS70230-2) at RT for 2 min.
639 Finally, eosin (Sigma, HT110216-500ML) was added at RT for 1 min and the slides were
640 washed in diH_2O for three times, followed by imaging with Aperio LV1 slide scanner (Leica).

641 For immunostaining, the spinal cord sections on the slides were incubated at 37 °C for
642 1 min, post-fixed once more in 4% PFA at RT for 15 min, and then permeabilized and blocked
643 with the blocking buffer (10% normal goat serum and 0.5% Triton X-100 in PBS) at RT for 1
644 h. The primary rat anti-GFAP antibody (Invitrogen, 13-0300) was subsequently included in the
645 blocking buffer at 4 °C overnight. The sections were washed with 0.3% Triton X-100 in PBS
646 for three times and the secondary goat anti-rat-Alexa Fluor 568 antibody (Life Technologies,
647 A11077) was added to the slide for 1 h at RT. After washed by 0.3% Triton X-100 in PBS for
648 three times, the spinal cord sections on the slides were mounted with coverslips using the
649 VECTASHIELD Antifade Mounting Medium with DAPI (Vector Laboratories, H1200) and
650 imaged by Dragonfly Spinning Disk Confocal Microscope (Andor) with a 20x/0.75 NA objective.
651

652 ***In situ* hybridization (ISH) and fluorescence *in situ* hybridization (FISH)**

653 ISH was performed as previously described[70]. Briefly, the mouse spinal cord sections were
654 treated with 10 μg/mL proteinase K (QIAGEN, 19131) at 37°C for 5 min and then post-fixed in
655 4% PFA at RT for 10 min. After washing and dehydration, DIG-labeled RNA probes at
656 approximately 1 μg/mL in hybridization buffer were incubated with the sections on the slides
657 at 65°C overnight. Afterwards, the slides were washed with 50% formamide (Sangon,
658 A600212) in 2x saline sodium citrate (SSC) (Invitrogen, AM9770) at 65°C for 30 min, followed
659 by incubation with 1 mg/mL Rnase A (Roche, 10109142001) at 37°C for 30 min. The slides
660 were then washed sequentially in 2x SSC at 60°C for 20 min, 0.2x SSC at 60°C for 20 min,
661 and 0.1x SSC at RT for 20 min. For ISH, the slides were incubated with anti-DIG-AP (Roche,
662 11093274910) at 4°C overnight, followed by washing and incubation with BM-purple (Roche,
663 11442074001) until dark purple color became visible.

664 The composition of the hybridization buffer: 50% (v/v) formamide; 10 mM Tris-HCl solution,
665 pH 8.0 (Sangon, B548127); 200 μg/mL yeast tRNA (ThermoFisher, AM7119); 10% (v/v)
666 dextran sulfate (Millipore, S4030); 1x Denhardt's solution (Sigma, D9905); 600 mM NaCl,
667 RNase-free (ThermoFisher, AM9760G); 0.25% SDS (ThermoFisher, AM9820); 1 mM EDTA

668 (0.5 M), pH 8.0, RNase-free (ThermoFisher, AM9261); Nuclease-free water (ThermoFisher,
669 AM9937).

670 For FISH, the procedure was similar to the ISH but the anti-DIG-POD antibody (Roche,
671 11207733910) was used for signal development. The slides were finally incubated with
672 TSA_Plus_Fluorescence Kits (Akoya, NEL745001KT) according to the manufacturer's
673 instruction and imaged.

674 For simultaneous detection of the immunofluorescence signals of GFAP with FISH, the
675 immunostaining was conducted after FISH images had been obtained. Antigen retrieval was
676 performed with Antigen Retrieval Solution (Solarbio, C1035) before the conventional
677 immunostaining procedure.

678 The RNA probes used in this study were adapted from the Allen Spinal Cord Atlas
679 (https://mousespinal.brain-map.org/), and synthesized with the DIG RNA labeling kit (Roche,
680 11277073910) following the procedure described in (Peng et al., 2016)[70]. The following
681 primers were used:

682 *Gfap* forward: 5'---GTGGATTTGGAGAGAAAGGTTG---3'

683 *Gfap* reverse: 5'---CTGGAGGTTGGAGAAAGTCTGT---3'

684 *Pla2g7* forward: 5'---AAGGTCGCCTCGACACTG---3'

685 *Pla2g7* reverse: 5'---TCAAAGGGTGACCCAGGA---3'

686 *Igfbp2* forward: 5'---ACAGTGATGACGACCACTCTGA---3'

687 *Igfbp2* reverse: 5'---CCTCTCTAACAGAAGCAAGGGA---3'

688

689 **Culture primary astrocytes from mouse pup brains**

690 Primary astrocytes were isolated from C57BL/6J newborn mice at postnatal day 2 (P2) as
691 previously described[71]. In brief, after removal of the meninges, mouse cortical tissues were
692 minced and digested sequentially with 0.05% DNase I (Sigma, DN-25) for 5 min and 0.05%
693 trypsin (Gibco, 15090-046) for 20 min at RT, followed by filtration through a 70-μm cell strainer
694 (FALCON, 352350) to remove undissociated tissues and debris. The filtrate was centrifuged
695 at 150 *g* for 10 min, and the cell pellet was resuspended after decanting the supernatant. The

696 harvested cells were plated into T-75 flasks coated with 50 μg/mL poly-L-Lysine, and
697 incubated at 37 °C with 5% CO_2 in an incubator. The growth medium (10% fetal bovine serum
698 and 2% penicillin-streptomycin in DMEM) was changed every other day. Upon the confluence
699 of the cells, oligodendrocyte progenitor cells (OPCs) could be detached by tapping the flask
700 and DNase I digestion (37 °C for 5 min). After completely removing the supernatant, the
701 remaining adherent cells were subsequently digested with 0.25% trypsin for 5 min. The cell
702 suspension was mixed with an equal volume of the growth medium to deactivate trypsin, and
703 centrifuged for collecting the pellet. Thereafter, the resuspended cells were subjected to two
704 rounds of incubation in bacterial grade plates for 20 and 90 min, respectively. This helped to
705 effectively remove the microglia as they are more prone to attach to the plate surface
706 compared with astrocytes. The supernatant was then transferred to a new T-75 flask, and
707 primary astrocytes were allowed to grow to confluence before use.
708

709 **Lentivirus production**

710 To generate lentivirus for infecting primary astrocytes, 293T cells were co-transfected with
711 target plasmid (pCDH-vector-flag or pCDH-*Igfbp2*-flag), psPAX2 and pMD2.G with a ratio of
712 4:3:1 in Opti-MEM (Gibco, 31985070) using Lipofectamine 2000 (Invitrogen, 11668). The
713 culture medium was collected at 48 h after transfection and passed through a 0.45-μm filter.
714 Viral particles were concentrated using the Lenti-X Concentrator (Clontech, 631232) and the
715 viral pellets were resuspended in PBS for astrocyte infection.
716

717 **The *in vitro* cell migration assay**

718 Primary cultures of mouse astrocytes were grown *in vitro* in the plates coated with 5 μg/mL
719 fibronectin (Sigma, F2006) for 4-5 days before they were infected with lentivirus. Three days
720 after infection, the astrocytes were treated with 10 μg/mL mitomycin C (Sigma, M5353) for 2
721 h to suppress cell proliferation and then the middle of the monolayered astrocytes was
722 scratched with a pipette tip to create a gap (cell-free area), which was traced and imaged at
723 0, 24 and 48 hours post scratch (hps) using phase contrast microscopy.

724

725 **Image acquisition, processing and quantification of light microscopy**

726 Brightfield images of H&E staining and ISH were acquired using the Aperio LV1 slide scanner
727 (Leica) and processed in ImageScope. FISH and immunofluorescence images were acquired
728 using the Dragonfly Spinning Disk Confocal Microscope (Andor) with a 20x/0.75 NA objective.
729 The 3D rendering of the GFAP$^+$-*Igfbp2*$^+$ astrocytes was performed in Imaris using the Surface
730 function. The images were processed and assembled into figures using Adobe Photoshop
731 2022 and Adobe Illustrator 2022.

732 For quantification of astrocytes, two regions of interest (ROIs) were drawn to outline the
733 left and right grey matter (GM) of each spinal cord section from three different animals (n = 6
734 ROIs for each time point). The number of DAPI, GFAP$^+$ or *Igfbp2*$^+$ cells within each ROI was
735 counted by ImageJ using the Analyze Particles function. And the GFAP$^+$/*Igfbp2*$^+$ double-
736 positive cells over DAPI were visually examined and manually counted. Statistical analysis
737 was determined by one-way analysis of variance (ANOVA) with Tukey's HSD post-hoc test at
738 $*p < 0.05$, $**p < 0.01$, and $***p < 0.001$. Error bars represent the standard error of the mean
739 (SEM).

740 For quantification of the gap size in the cell migration assay, the cell-free area was
741 delineated, with its size measured by ImageJ at 0, 24 and 48 hps. Six randomly-selected, non-
742 overlapping regions of the samples prepared independently in each group were included at
743 each time point for calculating the percentage of the gap area, using the following equation:
744 Relative gap size (%) = S/S_{0hps} x 100%, where S stands for the number of the pixels of the
745 cell-free area of a sample, and S_{0hps} is that of the same sample at 0 hps.

746

747 **Acquisition of mouse spinal cord sections for 10x Genomics Visium spatial RNA-seq**

748 Dissected spinal cords were washed with 1x PBS and subsequently embedded in Tissue-Tek
749 O.C.T. through a bath of dry ice and prechilled ethanol. Before sectioning, Visium slides and
750 samples were equilibrated to -20°C in the cryostat for at least 30 min. Four consecutive spinal
751 cord cryosections were cut at 20-μm thickness each and attached to one of the four capture

752 areas of the Visium Spatial Gene Expression slides (10x Genomics, 1000184). The slides
753 were stored individually in sealed containers at -80°C before library construction.
754
755 **Spatial transcriptomics library construction and sequencing**
756 The spatial transcriptomics library was constructed according to the Visium Spatial Gene
757 Expression Reagent Kits User Guide (10x Genomics, CG000239 Rev D). In brief, after H&E
758 staining and imaging, the spinal cord samples on the slides were permeabilized for 18 min,
759 which was determined based on the pre-tests using the tissue optimization kit (10x Genomics,
760 1000193). Thereafter, the tissue slides were reverse transcribed and amplified, producing
761 cDNAs containing the spatial barcodes. The amplified cDNAs were subjected to library
762 construction and sequenced with the Illumina NovaSeq 6000 system using a 150-bp paired-
763 end setting at a depth of 100k reads per spot.
764
765 **Data analyses of spatial transcriptomics**
766 **Pre-processing and quality control**
767 The raw Visium spatial RNA-seq data and histological H&E images were processed using the
768 Space Ranger pipeline (v.1.0.0, 10x Genomics) to align and summarize unique molecular
769 identifier (UMI) counts according to the reference genome “Mouse Genome mm10”.
770 To assess the quality of the spatial RNA-seq data, we grouped the SCI samples based
771 on the replicate batch and estimate the sample correlation coefficients. In brief, average
772 expression of each spinal cord section replicate was calculated and the Pearson correlation
773 coefficient (PCC) analysis was performed across all samples. The expressed genes, UMI
774 counts and mitochondrial levels were computed by Seurat (version 4.1.1)[72]. Gene expression
775 levels of all spatial spots were normalized and scaled using the ‘SCTransform’ function[73] and
776 merged by regressing out 'section' factors to create a single Seurat object for further analyses.
777 All the hemoglobin-related genes (due to infiltration of red blood cells from the damaged blood-
778 spinal cord barrier) were removed from the matrix before merging. Other potential confounding

779 effects including cell cycle, sequencing library size and percentage of mitochondria were
780 regressed out as well.
781
782 **Spatial cluster analysis**
783 The top 3,000 highly variable genes during SCI were identified and used for the subsequent
784 analysis. We computed 20 principal components (PCs) with 'runPCA' and constructed the
785 shared nearest neighborhood graph with 50 local neighbors of each pixel using the
786 'FindNeighbors' function. We used the Louvain clustering algorithm to optimize the modularity
787 of neighbors and the UMAP (Uniform Manifold Approximation and Projection) visualization at
788 the resolution of 0.25. Seven spatiotemporal clusters were recognized and classified into four
789 anatomic domains according to their spatial distributions and the identified signature genes:
790 white matter (WM), middle grey (MG), dorsal horn (DH) and ventral horn (VH).
791
792 **Evaluation of activity scores of gene sets**
793 Injury, proliferation and migration scores of the indicated gene sets were computed using the
794 function of 'AddModuleScore' in Seurat with gene sets extracted from published literatures or
795 defined by the enrichment analysis. Specifically, the injury score was calculated based on the
796 expression of the following 22 genes: *Adamts1*, *Atf3*, *Ccl2*, *Ccnd1*, *Cd68*, *Cebpd*, *Cyba*, *Fn1*,
797 *Gal*, *Gap43*, *Hmox1*, *Hspb1*, *Igfbp2*, *Jun*, *Junb*, *Fos*, *Lgals1*, *Neat1*, *Socs3*, *Tnc*, *S100a10*,
798 and *Timp1*; the proliferation score was calculated based on the expression of *Mki67*; and the
799 migration score was calculated based on the expression of the genes in the "positive
800 regulation of cell migration" gene ontology (GO) term.
801
802 **Differential expression gene (DEG) and GO term analyses**
803 For DEG analysis, 'FindAllMarkers' and 'FindMarkers' of Seurat were run with the following
804 parameters: logfc.threshold = 0.5, min.pct = 0.25 and method = "wilcoxon". GO term analysis
805 was done using the "clusterProfiler" R package[74]. The 'compareCluster' function was used for

806 gene list enrichment against all expressed genes by setting *p.* adjust < 0.01 or 0.05. The top
807 5 or 10 (*p*. adjust) terms were displayed by DotPlot.
808
809 **Gene co-expression analysis**
810 The WGCNA (weighted gene co-expression network analysis) package in R[75] was used to
811 measure co-expression networks across all the spatial spots. Genes expressed in over 100
812 spatial spots were selected and their average expression levels in each group of injury time
813 and anatomic domains were calculated. To calculate the adjacent matrix, the soft power of 18
814 was chosen with the WGCNA function 'pickSoftThreshold'. The module identification and
815 topological connectivity network were computed using the 'DynamicTreeCut' function with
816 min.module.size = 30, deep = 2 and mergeHeight = 0.15. The most connected genes in the
817 topological network of each module were defined as the hub genes and were visualized with
818 Cytoscape[76]. Ribosome-related genes were filtered manually to avoid overdominance in co-
819 expression analysis when displaying connectivity network of Co-expressed Gene Module
820 (CGM) 9. Enriched regulons of CGMs were determined using the hypergeometric test against
821 previously identified regulons of transcription factors (TFs) and the cutoff *p*. adjust (which was
822 calculated with the bonferroni multiple comparison correction of *p* value in hypergeometric test
823 by the number of modules) was set to < 0.05. Indices of significance were calculated by (0.05
824 - *p*. adjust)/0.05. The top 3 (ranked by significance index) regulons of gene modules were
825 displayed.
826
827 **Analysis of transcriptional regulons and regulon modules (RMs) with SCENIC (single-**
828 **cell regulatory network inference and clustering)**
829 The Python package "pyscenic"[28] was used to detect active transcription RMs. Briefly, the
830 spatial gene expression matrix was first filtered to exclude genes expressed in fewer than 0.1%
831 of all the spots. The gene-gene correlation matrix for module identification was computed with
832 the Random Forest based on the 'GRNBoost2' algorithm. Each module was further pruned to
833 only include genes that were present in the RcisTarget database with the 'prune2df' function.

834 Therefore, regulons consisting of the TFs and their transcriptional targets in the co-expression
835 module were detected finally. Overall, 515 regulons were found in this study and the regulon
836 scores were calculated by the 'AUCell' function. To evaluate the co-expression relationship of
837 the regulons, the top 20 regulons (based on the regulon specificity score, the RSS[77] for each
838 combination of anatomic domain and injury time was picked (147 regulons in total; less than
839 predicted due to redundant regulons), which were then used to compute their connectivity
840 specificity index (CSI) for each pair of regulons following the instruction in (Bass et al., 2013)[78].
841 Based on the CSI, 7 RMs were identified via hierarchical clustering. Activity score of each CSI
842 module was calculated by averaging the regulon scores within each module. Regulon modules
843 with PCC > 0.65 were visualized with Cytoscape[76].
844 For regulon analysis of the single-cell data of astrocytes, the same procedure was
845 followed and 433 regulons were identified. The scaled average activity was computed across
846 three spatial associated states and the top 10 regulons of each state (based on RSS) were
847 shown.
848
849 **Cell type deconvolution and identification of cell type-enriched DEGs**
850 To estimate the proportions of the cell types in each spatial spot, all the spots were
851 deconvoluted with the "Spatial eXpression R (spacexr)" package (version 2.0, formerly
852 RCTD[34]). For a better inclusiveness of diverse cell types, we imported and combined two
853 mouse spinal cord single-cell datasets[9,35] in the RCTD analysis. We further defined astrocytes
854 in the SCI single-cell data[9] into three subtypes (astrocyte-*Gfap*, -*Slc7a10* and -*Svep1*) with the
855 annotation by Rosenberg et al. (2018)[35] as the reference by label transfer[79]. The cell types in
856 the sham and injured spinal cords (up to 72 hpi) identified by Milich et al. (2021)[9] were used
857 to construct the spacexr reference. Finally, the percentage of different cell types for each spot
858 was calculated using 'run.RCTD' with "multi" mode (CELL_MIN_INSTANCE = 10, UMI_min =
859 (min(puck@UMI)-1), UMI_max = (max(puck@UMI)+1), fc_cutoff_reg = 1). For robust cell type
860 decomposition, confident sub_weight was used to evaluate the final proportions of different
861 cell types in all spots. Astrocytes-*Svep1* and dendritic cells were merged into the class of

862 “other cells” due to their extremely low presence in the overall spatial transcriptomic data and
863 were not considered in the subsequent analysis. In addition, excessive subtype classifications
864 showing scattered spatial distributions were merged and analyzed at the cell type level.
865 The DEGs of the indicated cell type were calculated with the ‘C-SIDE’ function[80]. For
866 analysis of astrocyte subtype-enriched DEGs, astrocytes-WM or -GM in the four replicates of
867 the +1.0 mm sections at 0 hpi were passed to C-SIDE with the parameters of
868 “cell_type_threshold = 1, weight_threshold = 0.9 and doublet_mode = F” and their spatial
869 localization was used as a function of the covariates.
870

871 **Spatial-aware cell-cell communication (SA-CCC) analysis**

872 The ligand_receptor (L_R) pair interaction information was extracted from CellChatDB.mouse
873 of CellChat[37]. To further pinpoint the L_R pair interactions between different cell-type pairs in
874 the spatial context, we binarized the L_R pair consensus matrix of each spatial spot based on
875 whether its value exceeded its assembly mean across all spots. Similarly, the cell-type pairs
876 were also binarized depending on their deconvolution proportions. To minimize the
877 interference from ubiquitous and/or ambiguous interactions from other cell types, the
878 proportions of neurons and oligodendrocytes were filtered by their mean values when
879 assessing the spatial interactions. Additionally, to exclude “false interaction” between spatially
880 nonadjacent cells, the cell-type pairs were eliminated if the Spearman rank correlation
881 coefficient of their deconvolution proportions was < -0.4. The spatial correlation between each
882 L_R pair and cell-type pair was calculated using the one-side Fisher’s exact test. When the *p*
883 value was < 0.001, the cell-type pair was considered to have a bona fide spatial cell-cell
884 interaction. The expression level of a specific L_R pair for an associated cell-type pair was
885 calculated by averaging the values of L_R pair geometric mean (GeoM) across their
886 colocalized pixels. The aggregated types of cell-cell interactions, the average expression
887 levels of all L_R pairs between indicated cell-type pairs and the -log10(GeoM of *p* values) at
888 each time point of SCI were visualized by igraph[81]. Only interactions between the cell-type
889 pairs that have over 10 shared positive spatial spots were shown. The SA-CCC results were

890 further applied to assess the cell-cell interactions identified in the SCI single-cell study[9] using
891 the CellChat with the default parameters. The SA-CCC analysis is accessible and searchable
892 in our interactive data exploration portal: *(will release to the public upon acceptance of the*
893 *paper)*.
894

895 **Re-analysis of the SCI single-cell datasets of the spatially-defined astrocytes**

896 To re-cluster the astrocytes in the SCI single-cell dataset[9], the single-cell matrix was
897 normalized and scaled using the 'SCTransform' function (var.to.regress =
898 c("orig.ident","S.Score","G2M.Score","percent_mt","percent_rp"), do.scale = TRUE). Cells
899 with low counts (< 2,500) were filtered. Ribosome- and mitochondria-related genes were
900 regressed out. The top 16 PCs, 40 k.param and resolution = 0.2 were used in the UMAP
901 analysis (Extended Data Fig. 9d). Two molecularly-defined subtypes of astrocytes-WM (*Gfap*$^{+}$)
902 and astrocytes-GM (*Slc7a10*$^{+}$) were identified, and the subsets of the RNA matrix of the
903 astrocytes were used in the subsequent analyses.

904 The spatially scaled data were used to extract the expression profiles of astrocytes-WM
905 in all the spots that contained astrocytes-WM based on the deconvolution result. The 317
906 astrocyte marker genes used in the cell type deconvolution analysis were retained. Scaled
907 expression was binarized into 1 and -1 based on the threshold = 0, which was used to estimate
908 the expression of each marker gene at the bulk level in the WM and the GM at all time points
909 of SCI. K-means clustering (k = 4) was employed to identify spatially-defined marker genes
910 for the SA groups of astrocytes in Fig. 4g.

911 To evaluate whether the SA-1 and SA-4 gene groups were able to distinguish astrocytes-
912 GMii from the rest astrocytes-WM, the astrocytes-*Gfap* (WM) defined in the SCI single-cell
913 study[9] were re-clustered using the maximum distance and the 'cutree' function based on the
914 scores of the SA-1 and SA-4 gene sets. The DEGs of the original astrocytes-WM and -GM as
915 well as the injury-induced astrocytes-GMii were identified and compared pairwise to reveal
916 their overlapping relationships (logfc.threshold = 0.5, *p*. adjust < 0.01). Surface marker

917 analysis was done by overlapping the surface genes downloaded from Cell Surface Protein
918 Atlas with astrocyte-GMii signature genes.
919
920 **Pseudotime analysis**
921 Trajectory inference was performed in low dimension data of the astrocytes-*Gfap* (WM),
922 including the astrocytes in the uninjured WM and the GM-relocated, WM-featured astrocytes
923 after injury, in the SCI single-cell study[9] using the slingshot package (v2.5.5)[42].
924
925 **Statistical information**
926 The exact statistical information of the comprehensive spatial transcriptomic analyses in this
927 study is specified in each related section of the Methods above or as indicated in the legends
928 of the relevant figures.
929
930 **Data and Materials Availability**
931 Raw data generated by SpaceRanger pipelines are available through the NODE project under
932 the accession number OEP003508. Our SCI spatial transcriptomic resources can be explored
933 at the SCI-ST web portal *(will release to the public upon acceptance of the paper)*. All other
934 data are available in the main text and the supplementary materials. All unique and stable
935 reagents generated in this study are available from the corresponding authors with a
936 completed Material Transfer Agreement (MTA).
937
938 **Supplemental Information**
939 Supplemental information includes Extended Data Fig. 1-13, Supplemental References 82-86,
940 and Supplemental Tables 1-6.

Acknowledgements

We thank Drs. J. Hu, Z. He, C. Zhang, and Misses. J Zhu and Z. Sun for assistance in mouse operation, Dr. Q. Wang for help with cryosection, Mr. G. Zhang for technical support with 10x Genomics Visium spatial RNA-seq, Dr. X. Sun for help with ISH, and Drs. W. Li, Y. Song, B. Zhou, P. Yu, C. Liu, Z. He, G. Bai, H. Liu and J. Yuan for comments and critical reading of the manuscript.

Fundings

This study was supported by grants from National Key R&D Program of China (2018YFA0801402 to G.P.); the National Natural Science Foundation of China (NSFC) (31970697 and 32270812 to Y.F., 32270854 to G.P., and 82071372 to A. L.); the Science and Technology Commission of Shanghai Municipality (201409003300, 20490712600 and 2019SHZDZX02 to Y.F.); the “Strategic Priority Research Program” of the Chinese Academy of Science (XDA16020404) to G. P.; Natural Science Foundation of Guangdong Province (2021A1515011231 to A.L. and 2019B151502054 to G.P.), the Outstanding Scholar Program of Bioland Laboratory (2018GZR110102002) and the Science and Technology Program of Guangzhou (202007030012) to A. L.

Author Contributions

AL, GP and YF conceived the research; ZW, SS, and YF designed the experiments; ZW, SS and TL performed the experiments and analyzed the data; AL, WY and YL contributed important reagents; ZL, JX and GP performed the bioinformatic analyses; ZW, ZL, TL, GC, KZ, GP, AL and YF interpreted the results; ZW, ZL, TL, GP and YF prepared the figures; ZW, ZL, TL, AL, GP and YF wrote the paper. All authors read and approved the final manuscript.

Competing Interests

The authors declare no competing interests.

965 **REFERENCES** *(≤50 references)*

966 1. Ahuja, C. S. *et al.* Traumatic spinal cord injury. *Nat. Rev. Dis. Primers.* **3**, 17018 (2017).

967 2. Courtine, G. & Sofroniew, M. V. Spinal cord repair: advances in biology and technology.
968 *Nat. Med.* **25**, 898–908 (2019).

969 3. Anjum, A. *et al.* Spinal Cord Injury: Pathophysiology, Multimolecular Interactions, and
970 Underlying Recovery Mechanisms. *Int. J. Mol. Sci.* **21**, 7533 (2020).

971 4. Zhang, K., Jiang, M. & Fang, Y. The Drama of Wallerian Degeneration: The Cast, Crew,
972 and Script. *Annu. Rev. Genet.* **55**, 93–113 (2021).

973 5. Okada, S. *et al.* Conditional ablation of Stat3 or Socs3 discloses a dual role for reactive
974 astrocytes after spinal cord injury. *Nat. Med.* **12**, 829–834 (2006).

975 6. Adams, K. L. & Gallo, V. The diversity and disparity of the glial scar. *Nat. Neurosci.* **21**,
976 9–15 (2018).

977 7. Noristani, H. N. *et al.* Spinal cord injury induces astroglial conversion towards neuronal
978 lineage. *Mol. Neurodegener.* **11**, 68 (2016).

979 8. Wang, J.-J. *et al.* Molecular Expression Profile of Changes in Rat Acute Spinal Cord
980 Injury. *Front. Cell. Neurosci.* **15**, 720271 (2021).

981 9. Milich, L. M. *et al.* Single-cell analysis of the cellular heterogeneity and interactions in the
982 injured mouse spinal cord. *J. Exp. Med.* **218**, e20210040 (2021).

983 10. Moor, A. E. & Itzkovitz, S. Spatial transcriptomics: paving the way for tissue-level systems
984 biology. *Curr. Opin. Biotechnol.* **46**, 126–133 (2017).

985 11. Williams, C. G., Lee, H. J., Asatsuma, T., Vento-Tormo, R. & Haque, A. An introduction
986 to spatial transcriptomics for biomedical research. *Genome Med.* **14**, 68 (2022).

987 12. Asp, M. *et al.* A Spatiotemporal Organ-Wide Gene Expression and Cell Atlas of the
988 Developing Human Heart. *Cell* **179**, 1647-1660.e19 (2019).

989 13. Maniatis, S. *et al.* Spatiotemporal dynamics of molecular pathology in amyotrophic lateral
990 sclerosis. *Science* **364**, 89–93 (2019).

991 14. Peng, G. *et al.* Molecular architecture of lineage allocation and tissue organization in
992 early mouse embryo. *Nature* **572**, 528–532 (2019).

993 15. Chen, W.-T. *et al.* Spatial Transcriptomics and In Situ Sequencing to Study Alzheimer's
994 Disease. *Cell* **182**, 976-991.e19 (2020).

995 16. Ortiz, C. *et al.* Molecular atlas of the adult mouse brain. *Sci. Adv.* **6**, eabb3446 (2020).

996 17. Fawkner-Corbett, D. *et al.* Spatiotemporal analysis of human intestinal development at
997 single-cell resolution. *Cell* **184**, 810-826.e23 (2021).

998 18. Rao, A., Barkley, D., França, G. S. & Yanai, I. Exploring tissue architecture using spatial
999 transcriptomics. *Nature* **596**, 211–220 (2021).

1000 19. Li, Z. & Peng, G. Spatial transcriptomics: new dimension of understanding biological
1001 complexity. *Biophysics Rep.* (2021) doi:10.52601/bpr.2021.210037.

1002 20. Ratz, M. *et al.* Clonal relations in the mouse brain revealed by single-cell and spatial
1003 transcriptomics. *Nat. Neurosci.* **25**, 285–294 (2022).

1004 21. Tavares-Ferreira, D. *et al.* Spatial transcriptomics of dorsal root ganglia identifies
1005 molecular signatures of human nociceptors. *Sci. Transl. Med.* **14**, eabj8186 (2022).

1006 22. Monje, M. Myelin Plasticity and Nervous System Function. *Annu. Rev Neurosci.* **41**, 61–
1007 76 (2018).

1008 23. Li, L. *et al.* The Specific Role of Reactive Astrocytes in Stroke. *Front. Cell Neurosci* **16**,
1009 850866 (2022).

1010 24. Willemsen, L. & Winther, M. P. Macrophage subsets in atherosclerosis as defined by
1011 single‐cell technologies. *J. Pathol.* **250**, 705–714 (2020).

1012 25. Langfelder, P. & Horvath, S. WGCNA: an R package for weighted correlation network
1013 analysis. *BMC Bioinformatics* **9**, 559 (2008).

1014 26. Macdonald, C. D. *et al.* Cytokine-induced cysteine- serine-rich nuclear protein-1
1015 (CSRNP1) selectively contributes to MMP1 expression in human chondrocytes. *PLOS*
1016 *ONE* **13**, e0207240 (2018).

1017 27. von Scheidt, M. *et al.* Transcription Factor MAFF (MAF Basic Leucine Zipper
1018 Transcription Factor F) Regulates an Atherosclerosis Relevant Network Connecting
1019 Inflammation and Cholesterol Metabolism. *Circulation* **143**, 1809–1823 (2021).

1020 28. Aibar, S. *et al.* SCENIC: single-cell regulatory network inference and clustering. *Nat.*
1021 *Methods* **14**, 1083–1086 (2017).

1022 29. Zhou, Q., Wang, S. & Anderson, D. J. Identification of a Novel Family of Oligodendrocyte
1023 Lineage-Specific Basic Helix–Loop–Helix Transcription Factors. *Neuron* **25**, 331–343
1024 (2000).

1025 30. Pierrot, N. Amyloid precursor protein regulates SREBP-mediated neuronal lipid
1026 homeostasis in mice and humans. *Alzheimers Dement.* **7**, S572 (2011).

1027 31. Shaulian, E. & Karin, M. AP-1 in cell proliferation and survival. *Oncogene* **20**, 2390–2400
1028 (2001).

1029 32. Liu, T., Zhang, L., Joo, D. & Sun, S.-C. NF-κB signaling in inflammation. *Sig. Transduct.*
1030 *Target. Ther.* **2**, 17023 (2017).

1031 33. Mogensen, T. H. IRF and STAT Transcription Factors - From Basic Biology to Roles in
1032 Infection, Protective Immunity, and Primary Immunodeficiencies. *Front. Immunol.* **9**,
1033 3047 (2019).

1034 34. Cable, D. M. *et al.* Robust decomposition of cell type mixtures in spatial transcriptomics.
1035 *Nat. Biotechnol.* **40**, 517–526 (2022).

1036 35. Rosenberg, A. B. *et al.* Single-cell profiling of the developing mouse brain and spinal cord
1037 with split-pool barcoding. *Science* **360**, 176–182 (2018).

1038 36. Köhler, S., Winkler, U. & Hirrlinger, J. Heterogeneity of Astrocytes in Grey and White
1039 Matter. *Neurochem. Res.* **46**, 3–14 (2019).

1040 37. Jin, S. *et al.* Inference and analysis of cell-cell communication using CellChat. *Nat.*
1041 *Commun.* **12**, 1088 (2021).

1042 38. Escartin, C. *et al.* Reactive astrocyte nomenclature, definitions, and future directions. *Nat.*
1043 *Neurosci.* **24**, 1–14 (2021).

1044 39. Sidoryk-wegrzynowicz, M., Wegrzynowicz, M., Lee, E., Bowman, A. B. & Aschner, M.
1045 Role of Astrocytes in Brain Function and Disease. *Toxicol. Pathol.* **39**, 115–123 (2011).

1046 40. Molofsky, A. V. *et al.* Astrocytes and disease: a neurodevelopmental perspective. *Genes*
1047 *Dev.* **26**, 891–907 (2012).

1048 41. Stogsdill, J. A. *et al.* Astrocytic neuroligins control astrocyte morphogenesis and
1049 synaptogenesis. *Nature* **551**, 192–197 (2017).

1050 42. Street, K. *et al.* Slingshot: cell lineage and pseudotime inference for single-cell
1051 transcriptomics. *BMC Genomics* **19**, 477 (2018).

1052 43. Khan, S. IGFBP-2 Signaling in the Brain: From Brain Development to Higher Order Brain
1053 Functions. *Front. Endocrinol. (Lausanne)* **10**, 822 (2019).

1054 44. Li, T. *et al.* IGFBP2: integrative hub of developmental and oncogenic signaling network.
1055 *Oncogene* **39**, 2243–2257 (2020).

1056 45. Yau, S. W., Azar, W. J., Sabin, M. A., Werther, G. A. & Russo, V. C. IGFBP-2 - taking
1057 the lead in growth, metabolism and cancer. *J. Cell Commun. Signal.* **9**, 125–142 (2015).

1058 46. Kaufmann, M. *et al.* Identification of early neurodegenerative pathways in progressive
1059 multiple sclerosis. *Nat. Neurosci.* **25**, 944–955 (2022).

1060 47. Anderson, M. A. *et al.* Astrocyte scar formation aids central nervous system axon
1061 regeneration. *Nature* **532**, 195–200 (2016).

1062 48. Gong, L. *et al.* Spatiotemporal Dynamics of the Molecular Expression Pattern and
1063 Intercellular Interactions in the Glial Scar Response to Spinal Cord Injury. *Neurosci. Bull.*
1064 (2022) doi:10.1007/s12264-022-00897-8.

1065 49. Sathyamurthy, A. *et al.* Massively Parallel Single Nucleus Transcriptional Profiling
1066 Defines Spinal Cord Neurons and Their Activity during Behavior. *Cell Rep.* **22**, 2216–
1067 2225 (2018).

1068 50. Zeisel, A. *et al.* Molecular Architecture of the Mouse Nervous System. *Cell* **174**, 999-
1069 1014.e22 (2018).

1070 51. Li, C. *et al.* Temporal and spatial cellular and molecular pathological alterations with
1071 single-cell resolution in the adult spinal cord after injury. *Signal Transduct. Target. Ther.*
1072 **7**, 65 (2022).

1073 52. Matson, K. J. E. *et al.* Single cell atlas of spinal cord injury in mice reveals a pro-
1074 regenerative signature in spinocerebellar neurons. *Nat. Commun.* **13**, 5628 (2022).

1075 53. Denisenko, E. *et al.* Systematic assessment of tissue dissociation and storage biases in
1076 single-cell and single-nucleus RNA-seq workflows. *Genome Biol.* **21**, 130 (2020).

1077 54. Yoon, H., Walters, G., Paulsen, A. R. & Scarisbrick, I. A. Astrocyte heterogeneity across
1078 the brain and spinal cord occurs developmentally, in adulthood and in response to
1079 demyelination. *PLOS ONE* **12**, e0180697 (2017).

1080 55. Hasel, P., Rose, I. V. L., Sadick, J. S., Kim, R. D. & Liddelow, S. A. Neuroinflammatory
1081 astrocyte subtypes in the mouse brain. *Nat. Neurosci.* **24**, 1475–1487 (2021).

1082 56. Renault-Mihara, F. *et al.* Spinal cord injury: Emerging beneficial role of reactive
1083 astrocytes' migration. *Int. J. Biochem. Cell Biol.* **40**, 1649–1653 (2008).

1084 57. White, R. E. & Jakeman, L. B. Don't fence me in: harnessing the beneficial roles of
1085 astrocytes for spinal cord repair. *Restor. Neurol. Neurosci.* **26**, 197–214 (2008).

1086 58. Lukovic, D. *et al.* Concise Review: Reactive Astrocytes and Stem Cells in Spinal Cord
1087 Injury: Good Guys or Bad Guys? *Stem Cells* **33**, 1036–1041 (2015).

1088 59. Bradbury, E. J. & Burnside, E. R. Moving beyond the glial scar for spinal cord repair. *Nat.*
1089 *Commun.* **10**, 3879 (2019).

1090 60. Fischer, I., Dulin, J. N. & Lane, M. A. Transplanting neural progenitor cells to restore
1091 connectivity after spinal cord injury. *Nat. Rev. Neurosci.* **21**, 366–383 (2020).

1092 61. Zipser, C. M. *et al.* Cell-based and stem-cell-based treatments for spinal cord injury:
1093 evidence from clinical trials. *Lancet Neurol.* **21**, 659–670 (2022).

1094 62. Okada, S., Hara, M., Kobayakawa, K., Matsumoto, Y. & Nakashima, Y. Astrocyte
1095 reactivity and astrogliosis after spinal cord injury. *Neurosci. Res.* **126**, 39–43 (2018).

1096 63. Tsai, H.-H. *et al.* Regional Astrocyte Allocation Regulates CNS Synaptogenesis and
1097 Repair. *Science* **337**, 358–362 (2012).

1098 64. Jeong, E. Y. *et al.* Enhancement of IGF-2-induced neurite outgrowth by IGF-binding
1099 protein-2 and osteoglycin in SH-SY5Y human neuroblastoma cells. *Neurosci. Lett.* **548**,
1100 249–254 (2013).

1101 65. Khan, S. *et al.* IGFBP2 Plays an Essential Role in Cognitive Development during Early
1102 Life. *Adv. Sci. (Weinh)* **6**, 1901152 (2019).

1103 66. Caldwell, A. L. M. *et al.* Aberrant astrocyte protein secretion contributes to altered
1104 neuronal development in multiple models of neurodevelopmental disorders. *Nat.*
1105 *Neurosci.* **25**, 1163–1178 (2022).

1106 67. Reshamwala, R. *et al.* Induction of Complete Transection-Type Spinal Cord Injury in Mice.
1107 *J. Vis. Exp.* **159**, 10.3791/61131 (2020).

1108 68. Basso, D. M. *et al.* Basso Mouse Scale for Locomotion Detects Differences in Recovery
1109 after Spinal Cord Injury in Five Common Mouse Strains. *J. Neurotrauma.* **23**, 635–659
1110 (2006).

1111 69. Martinov, T., Mack, M., Sykes, A. & Chatterjea, D. Measuring Changes in Tactile
1112 Sensitivity in the Hind Paw of Mice Using an Electronic von Frey Apparatus. *J. Vis. Exp.*
1113 **82**, e512512 (2013).

1114 70. Peng, G. *et al.* Spatial Transcriptome for the Molecular Annotation of Lineage Fates and
1115 Cell Identity in Mid-gastrula Mouse Embryo. *Dev. Cell* **36**, 681–697 (2016).

1116 71. Güler, B. E., Krzysko, J. & Wolfrum, U. Isolation and culturing of primary mouse
1117 astrocytes for the analysis of focal adhesion dynamics. *STAR Protoc.* **2**, 100954 (2021).

1118 72. Hao, Y. *et al.* Integrated analysis of multimodal single-cell data. *Cell* **184**, (2021).

1119 73. Hafemeister, C. & Satija, R. Normalization and variance stabilization of single-cell RNA-
1120 seq data using regularized negative binomial regression. *Genome Biol.* **20**, 296 (2019).

1121 74. Yu, G., Wang, L.-G., Han, Y. & He, Q.-Y. clusterProfiler: an R Package for Comparing
1122 Biological Themes Among Gene Clusters. *OMICS.* **16**, 284–287 (2012).

1123 75. Langfelder, P. & Horvath, S. WGCNA: an R package for weighted correlation network
1124 analysis. *BMC Bioinformatics* **9**, 559 (2008).

1125 76. Shannon, P. Cytoscape: A Software Environment for Integrated Models of Biomolecular
1126 Interaction Networks. *Genome Res.* **13**, 2498–2504 (2003).

1127 77. Suo, S. *et al.* Revealing the Critical Regulators of Cell Identity in the Mouse Cell Atlas.
1128 *Cell Rep.* **25**, 1436-1445.e3 (2018).

1129 78. Bass, J. I. F. *et al.* Using networks to measure similarity between genes: association
1130 index selection. *Nat. Methods* **10**, 1169–1176 (2013).

1131 79. Stuart, T. *et al.* Comprehensive Integration of Single-Cell Data. *Cell* **177**, 1888-1902.e21
1132 (2019).

1133 80. Cable, D. M. *et al.* Cell type-specific inference of differential expression in spatial
1134 transcriptomics. *Nat. Methods* **19**, 1076–1087 (2022).

1135 81. Csárdi, G. & Nepusz, T. The igraph software package for complex network research.
1136 *InterJournal, complex systems* **1695**, 1–9 (2006).

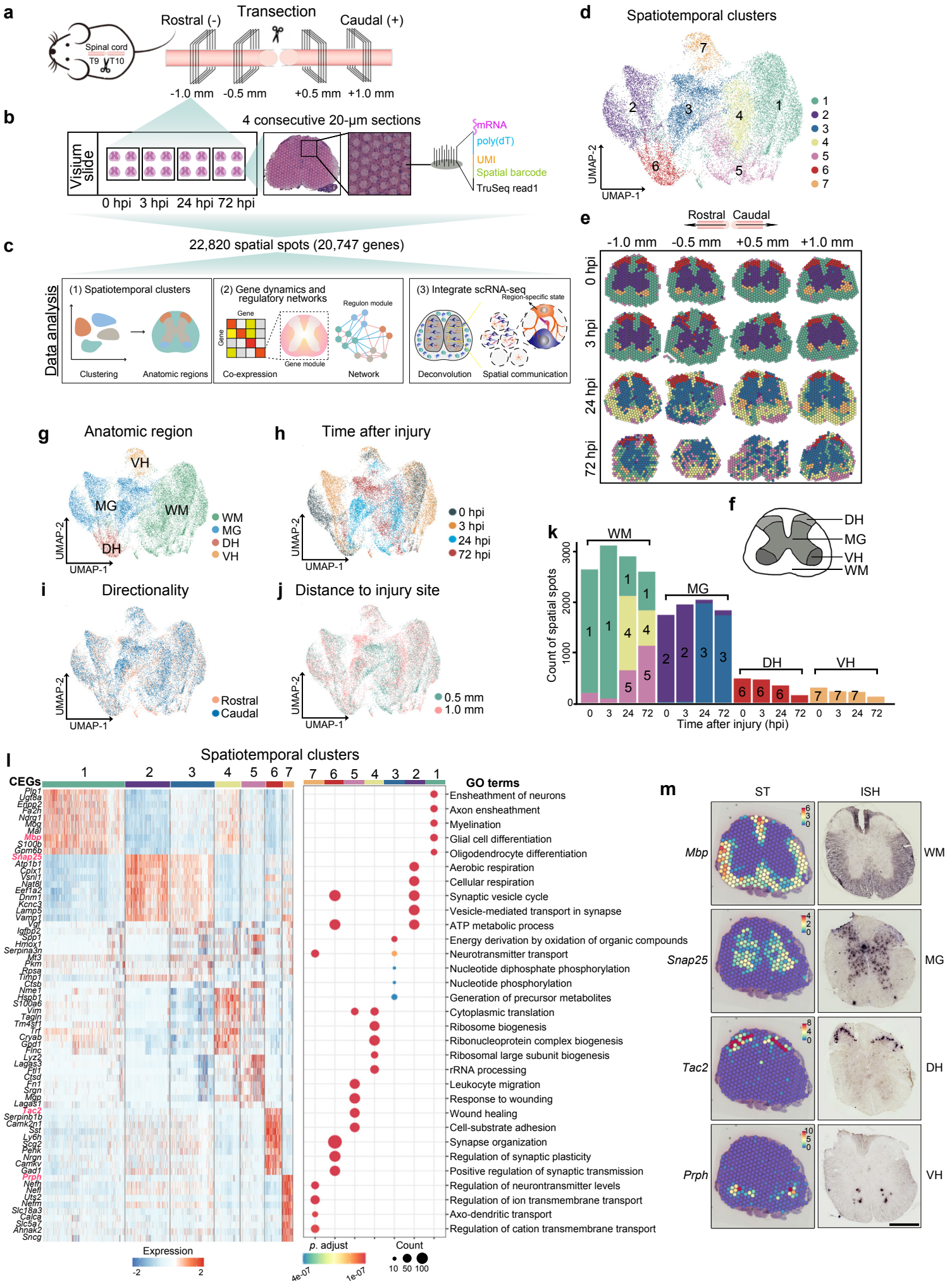
a
Rostral (-)
Transection
Caudal (+)
Spinal cord
T9
T10
-1.0 mm
-0.5 mm
+0.5 mm
+1.0 mm
b
4 consecutive 20-µm sections
Visium slide
0 hpi
3 hpi
24 hpi
72 hpi
mRNA
poly(dT)
UMI
Spatial barcode
TruSeq read1
c
22,820 spatial spots (20,747 genes)
Data analysis
(1) Spatiotemporal clusters
Clustering
Anatomic regions
(2) Gene dynamics and regulatory networks
Gene
Gene module
Regulon module
Co-expression
Network
(3) Integrate scRNA-seq
Region-specific state
Deconvolution
Spatial communication
d
Spatiotemporal clusters
UMAP-1
UMAP-2
e
Rostral
Caudal
-1.0 mm
-0.5 mm
+0.5 mm
+1.0 mm
0 hpi
3 hpi
24 hpi
72 hpi
f
DH
MG
VH
WM
g
Anatomic region
VH
MG
WM
DH
h
Time after injury
0 hpi
3 hpi
24 hpi
72 hpi
i
Directionality
Rostral
Caudal
j
Distance to injury site
0.5 mm
1.0 mm
k
Count of spatial spots
Time after injury (hpi)
l
Spatiotemporal clusters
CEGs
Expression
GO terms
Ensheathment of neurons
Axon ensheathment
Myelination
Glial cell differentiation
Oligodendrocyte differentiation
Aerobic respiration
Cellular respiration
Synaptic vesicle cycle
Vesicle-mediated transport in synapse
ATP metabolic process
Energy derivation by oxidation of organic compounds
Neurotransmitter transport
Nucleotide diphosphate phosphorylation
Nucleotide phosphorylation
Generation of precursor metabolites
Cytoplasmic translation
Ribosome biogenesis
Ribonucleoprotein complex biogenesis
Ribosomal large subunit biogenesis
rRNA processing
Leukocyte migration
Response to wounding
Wound healing
Cell-substrate adhesion
Synapse organization
Regulation of synaptic plasticity
Positive regulation of synaptic transmission
Regulation of neurotransmitter levels
Regulation of ion transmembrane transport
Axo-dendritic transport
Regulation of cation transmembrane transport
p. adjust
Count
m
ST
ISH
Mbp
Snap25
Tac2
Prph
WM
MG
DH
VH

Figure 2 - SCI ST

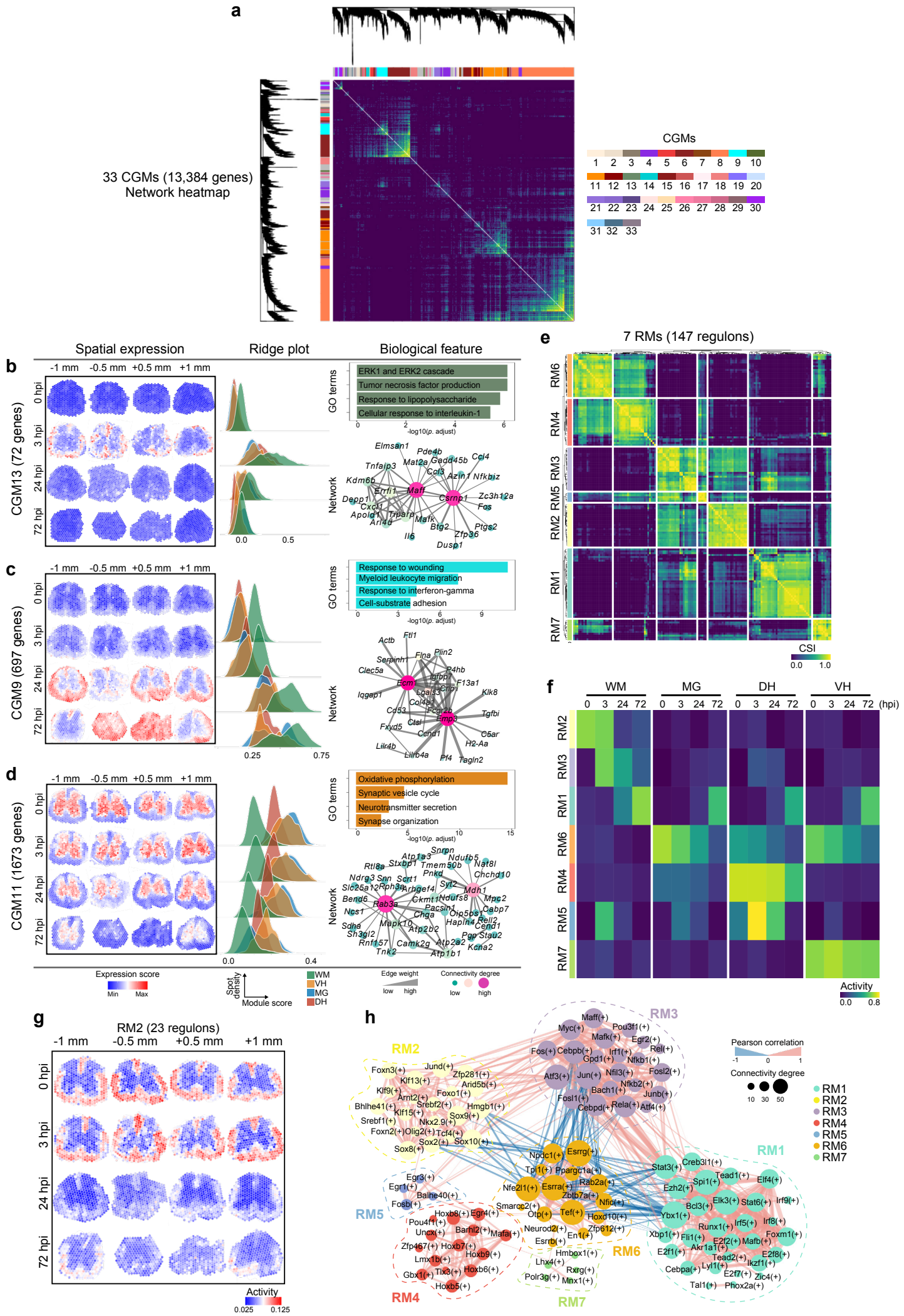

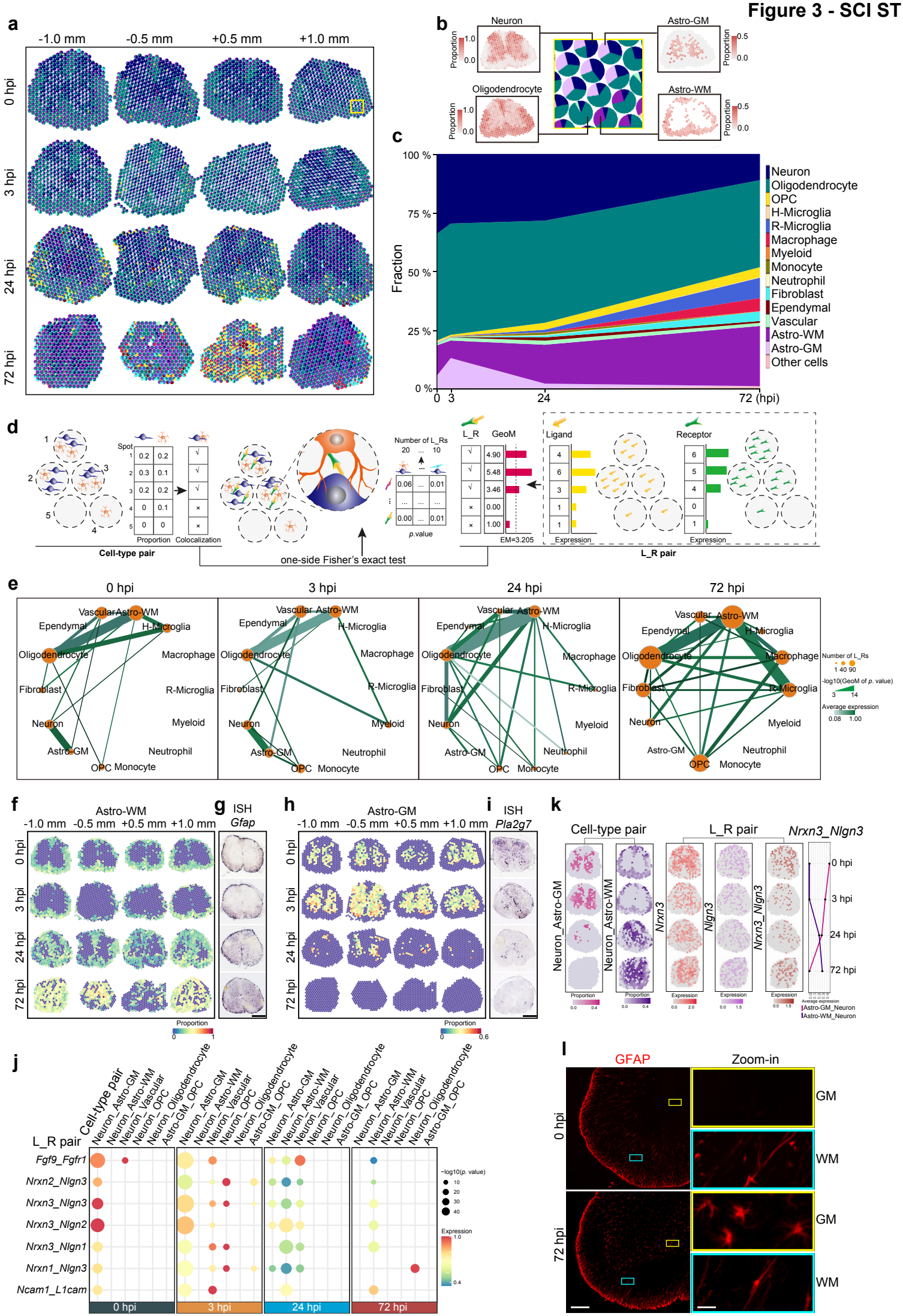
a
-1.0 mm
-0.5 mm
+0.5 mm
+1.0 mm
0 hpi
3 hpi
24 hpi
72 hpi
b
Neuron
Astro-GM
Oligodendrocyte
Astro-WM
Proportion
c
Fraction
100 %
75 %
50 %
25 %
0 %
0
3
24
72 (hpi)
Neuron
Oligodendrocyte
OPC
H-Microglia
R-Microglia
Macrophage
Myeloid
Monocyte
Neutrophil
Fibroblast
Ependymal
Vascular
Astro-WM
Astro-GM
Other cells
d
Spot
Proportion
Colocalization
Cell-type pair
Number of L_Rs
p.value
one-side Fisher's exact test
L_R
GeoM
EM=3.205
Ligand
Receptor
Expression
L_R pair
e
0 hpi
3 hpi
24 hpi
72 hpi
Vascular
Astro-WM
Ependymal
H-Microglia
Oligodendrocyte
Macrophage
Fibroblast
R-Microglia
Neuron
Myeloid
Astro-GM
Neutrophil
OPC
Monocyte
Number of L_Rs
-log10(GeoM of p. value)
Average expression
f
Astro-WM
-1.0 mm
-0.5 mm
+0.5 mm
+1.0 mm
g
ISH
Gfap
h
Astro-GM
i
ISH
Pla2g7
k
Cell-type pair
L_R pair
Nrxn3_Nlgn3
Neuron_Astro-GM
Neuron_Astro-WM
Nrxn3
Nlgn3
Nrxn3_Nlgn3
Proportion
Expression
Average expression
Astro-GM_Neuron
Astro-WM_Neuron
j
Cell-type pair
L_R pair
Fgf9_Fgfr1
Nrxn2_Nlgn3
Nrxn3_Nlgn3
Nrxn3_Nlgn2
Nrxn3_Nlgn1
Nrxn1_Nlgn3
Ncam1_L1cam
-log10(p. value)
Expression
0 hpi
3 hpi
24 hpi
72 hpi
l
GFAP
Zoom-in
GM
WM
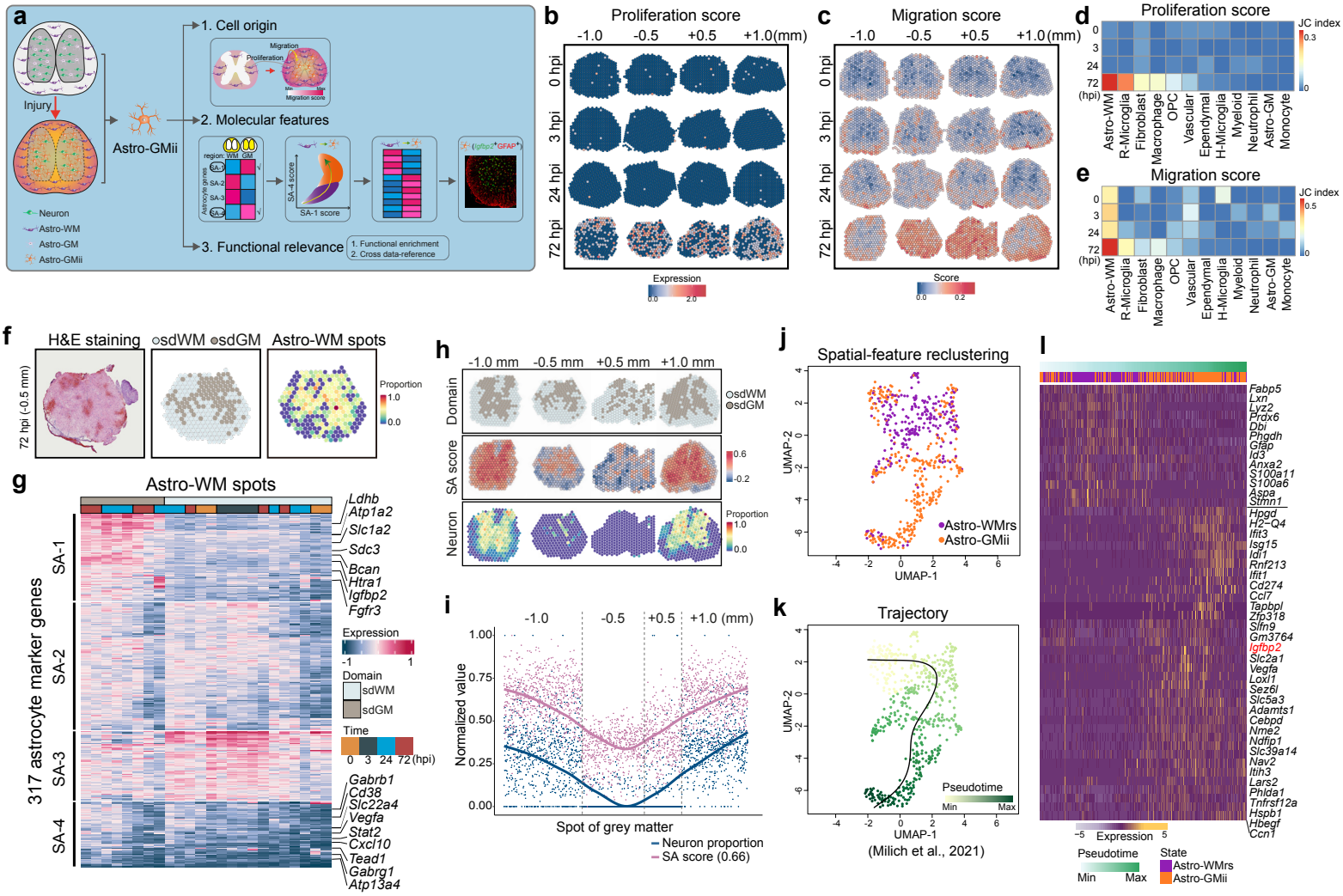
Figure 4 - SCI ST